



# **State of the Art in Scale Down for Dissolved Oxygen Transport**

## **Phase 1b Report**

**Radu Cimpeanu,  
Glenn Gaudette,  
Daniel Harris,  
Simon Hubbard,  
Luke Perreault.**

**Version 1 August 2023**

## Authors

This report and the work described herein has been executed as a project under the Cultivated Meat Modelling Consortium by the following participants:

Dr. Radu Cimpanu  
Mathematics Institute  
University of Warwick  
United Kingdom  
[radu.cimpanu@warwick.ac.uk](mailto:radu.cimpanu@warwick.ac.uk)  
<https://warwick.ac.uk/fac/sci/math/people/staff/cimpanu/>  
<https://www.raducimpanu.com/>

Prof. Glenn R. Gaudette  
John W. Kozarich '71 Inaugural Chair  
Boston College Department of Engineering  
[glenn.gaudette@bc.edu](mailto:glenn.gaudette@bc.edu)

Prof. Daniel M. Harris  
Assistant Professor of Engineering  
School of Engineering  
Brown University  
[daniel\\_harris3@brown.edu](mailto:daniel_harris3@brown.edu)  
<https://sites.brown.edu/harrislab/>

Dr. Simon Hubbard  
Owner & Lead Engineer  
Upstream Applied Science Ltd  
[simon@upstream-applied-science.com](mailto:simon@upstream-applied-science.com)  
[www.upstream-applied-science.com](http://www.upstream-applied-science.com)

Dr. Luke Perreault  
Visiting Assistant Professor of Engineering & Core Fellow  
Department of Engineering  
Boston College  
[luke.perreault@bc.edu](mailto:luke.perreault@bc.edu)

## Executive Summary

Merck KGaA, Darmstadt, Germany, are keen to further understand cell viability discrepancies observed between 1 millilitre microtiter plate and 15-25 milliliter TPP tube growth setups. The transfer of dissolved oxygen through the gas-liquid interface is believed to be a significant cause of the discrepancy.

In this Phase 1b activity a combination of measurements and modelling approaches have been developed and used to indicate the potential for dissolved oxygen transfer to be responsible for the observed discrepancies. Measurements indicate that mismatches in the mass transfer coefficient  $k_L a$  exist between the 96 well plates and TPP tubes studied here within the range of operating parameters (fill level, fill liquid, agitation RPM) considered. It is therefore plausible that oxygen mass transfer is responsible for the observed cell viability differences, depending on the operation parameters employed.

Computational fluid dynamics modelling of the hydrodynamics and mass transfer performance of the well plates and TPP tubes was performed using the open source framework Basilisk. Good prediction of the mass transfer coefficient  $k_L a$  across the parameter space were obtained, in addition to prediction of mixing times and shear stresses which may be of value in cases where cell viability discrepancies exist under equivalent mass transfer conditions.

In addition, progressively complex first principles models of the dynamics of the gas-liquid interface have been developed, providing fast predictive capability of the area of the interface under specific operating conditions for both well plates and TPP tubes. Good agreement was found for the vertical extent of the gas liquid interface ("interface height") with the experiments performed.

Recommendations for subsequent activities include:

- Further examination of operating parameters for which well plate and TPP tube cell viability discrepancies were observed, and to compare to the data generated here to ascertain if differences in the mass transfer coefficient  $k_L a$  could be responsible.
- Development of the dynamic technique for measuring the mass transfer coefficient  $k_L a$  to reduce both additional vibrations and variability in results across wells and between runs.
- Development of the Basilisk methodology to improve the accuracy of representing the forces at the gas-liquid-solid contact line.
- Extension of the first principles model to include a mass transfer prediction, with the potential to provide a generic, small scale, mass transfer prediction capability.
- Consideration of the broader scale application of modeling to ascertain the requirements for specific development of the tools used here, or to include additional modeling capabilities.



## 1. Introduction

This report describes the approach and results of measuring and simulating the oxygen mass transfer performance of orbitally shaken well plates and TPP tubes and some of the associated hydrodynamic behaviour. Additionally simulation results consider the mixing time and shear stress experienced by non-inertial particles, representative of cells.

The motivation for this activity is to provide some insight in to cell growth performance differences observed between 96 well plates and TPP tubes, with the oxygen mass transfer performance considered to be the most likely cause. The previous activity to this work, under Phase 1a, suggested mixing time and cell stress to be alternate candidates for the observed cell growth difference, prompting a preliminary assessment in this work.

There are three main sections to this work, each reported in separate sections: Section 2 describes the measurement techniques and results; Section 3, the development and use of bespoke models to predict gas-liquid interface characteristics; Section 4, the background and use of the open source computational fluid dynamics software Basilisk to predict mass transfer, mixing times and shear stress.

A summary of the work and recommendations for next steps is provided in Section 5.

## 2. Measurements

### 2.1. Overview

The objective of this section of the project was to determine experimental parameters for air-liquid interfacial height and oxygen transport under a range of different orbital velocities. These data can then be employed to investigate accuracy of computational models developed in this project. This information is pertinent to bioreactor design to determine metrics to increase oxygen transport rate ( $k_L a$ ) in culture, while attempting to minimize flow-induced shear force that can be detrimental to cell survival.

### 2.2. Methodologies

#### 2.2.1. Media and Reagent Preparation

MilliQ (MilliporeSigma, Burlington MA, USA) ultra-pure deionized water was used for all water analysis. Water measurements were conducted as technical controls, to validate accuracy of interfacial area and oxygen mass transport measurements. A custom DMEM/F12 formulation was provided by MilliporeSigma for the media analyses. Briefly, the DMEM/F12 basal media without phenol red was stored in powder form at 4° centigrade, and reconstituted in MilliQ water. Reconstituted media was stored at 4° centigrade for experimental use for up to 1 week.

The physical properties of the basal media and deionised water were measured for use in the bespoke and Basilisk models. The values and screenshots of measurement equipment are shown in Figure 2.1.

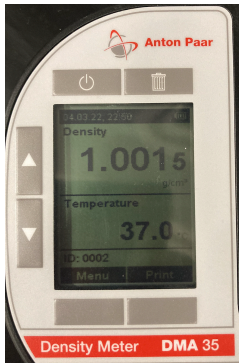
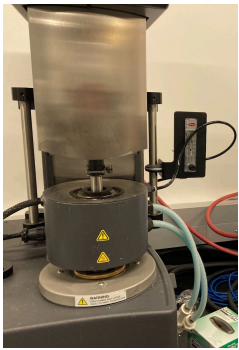

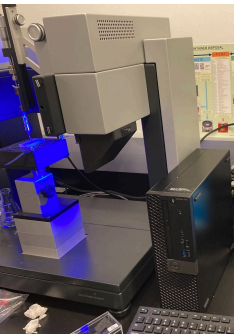
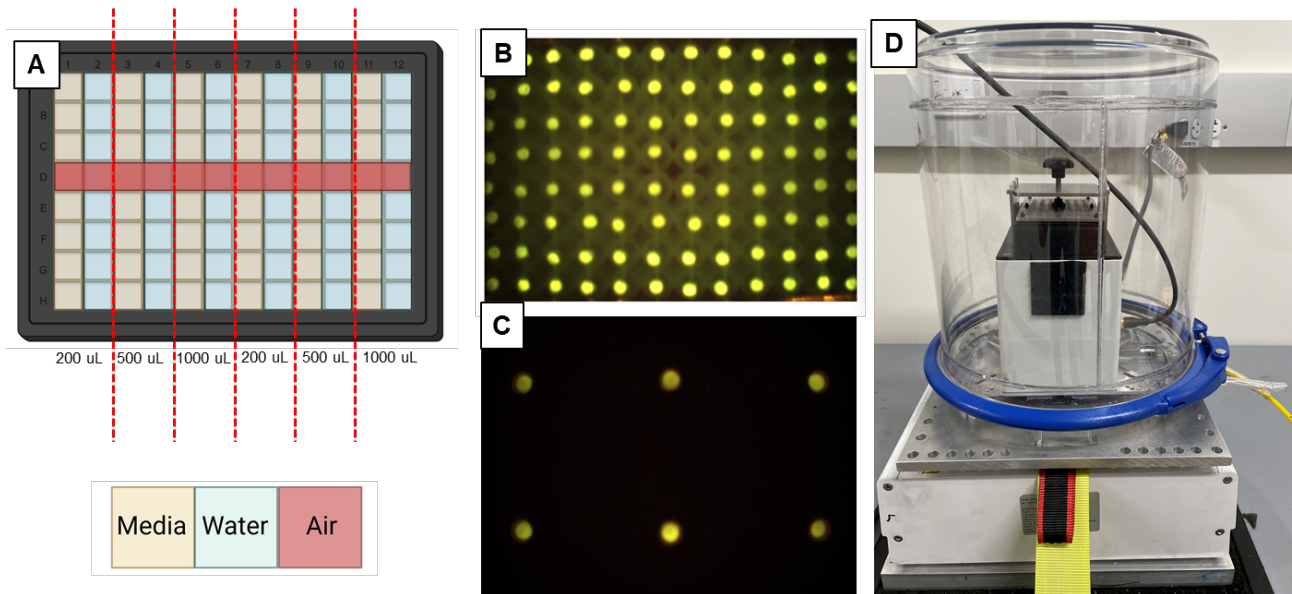
				
	<b>Density [kg/m<sup>3</sup>]</b>	<b>Viscosity [mPa.s]</b>	<b>Surface Tension [N/m]</b>	<b>PPE Contact Angle [degs]</b>
<b>Media</b>	1002	0.831	69.75	98.5
<b>Water</b>	993.3	0.691	69.60	102.1

Figure 2.1: Measurement equipment and measured values for the media and water physical properties.



**Figure 2.2: Experimental set up and equipment for oxygen transport analysis. A) 96-well plate sample arrangement. Water and media are staggered, and 200 $\mu$ L, 500 $\mu$ L, and 1000 $\mu$ L volumes are dispersed across the plate. B) 96-well plate sample fluorescence image used for oxygen analysis. C) Sample image of 6 conical tubes with fluorescent sensors used for analysis. D) Equipment used for oxygen transport experiments. An environmental chamber sits on a custom-modified orbital shaker, with VisiSens system secured inside. Computer interface cord exits out the top of the system and gas tubing is used to flow nitrogen or room air into the chamber continuously.**

### 2.2.2. Preparation of 96 Deep-Well Plates for Testing

Oxygen 96-well deep well plates (Corning Inc, Corning, NY, USA) were custom-modified by PreSens Precision Sensing GmbH (Regensburg, Germany) with prototype dissolved oxygen (DO) sensors (specifically, Oxygen Sensor Foil SF-RPSu4) that fluoresce under near-UV visible blue light (>390nm, exact wavelength is proprietary to PreSens), with fluorescent intensity correlating to oxygen content [1]. Circular foils ~3-4mm in diameter are adhered to the transparent bottom of each well, permitting analysis of oxygen content at the base.

Media and water were filled into each column of the plate, with row D (4<sup>th</sup> row) left empty to permit measurements of air oxygenation across the plate. Media and water were filled into side-by-side columns, at different fill volumes (200 $\mu$ L, 500 $\mu$ L, and 1000 $\mu$ L) to gauge the impact of volume on oxygen mass transfer. The physical set-up of the well is shown in Figure 2.2A, and the fluorescent foil visualization is shown in Figure 2.2B. Once prepared, the plate was allowed to equilibrate to room temperature before analysis. Volumes were determined empirically, evaluating the maximum volume that could be assessed before spilling at high speeds occurred. Plates and sensors were reused for experiments no more than 3 times, and flushed thoroughly with water and dried in the dark prior to reuse.

### 2.2.3. Preparation of 50mL Conical Tubes for Testing

As with deep well plates, PreSens oxygen sensor foils were custom-affixed to TPP TubeSpin bioreactor tubes (MilliporeSigma), at the base of each tube (Figure 2.2C). Tubes were filled with either 10mL or 20mL of DMEM/F12 basal media or MilliQ water. Once prepared, tubes were allowed to equilibrate to room temperature before analysis. As with deep-well plates, evaluated volumes were determined

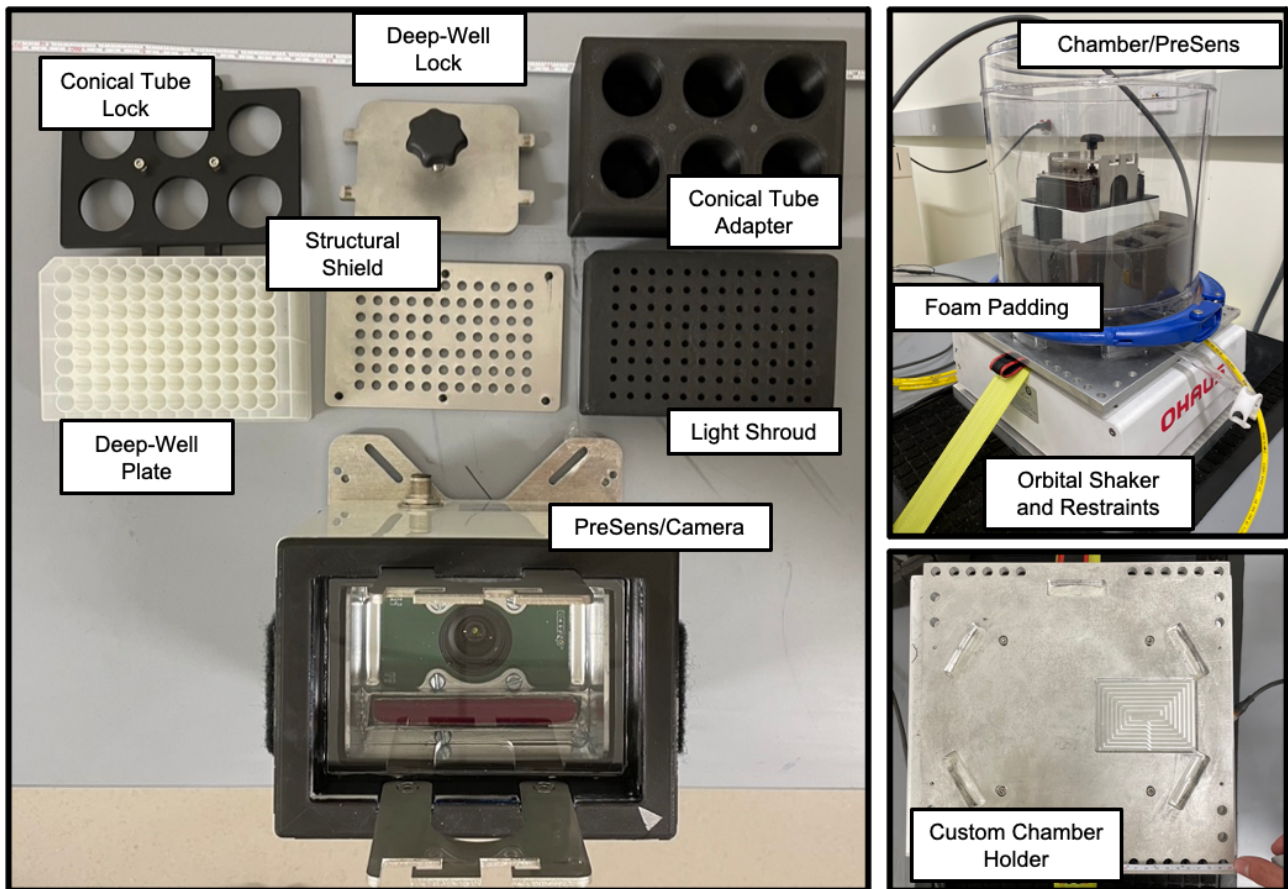


Figure 2.3: Overview of equipment used for oxygen data collection. The VisiSens (PreSens/Camera) system is modular, with adaptors to facilitate deep-well and conical tube configurations to be mounted above the camera. The orbital shaker is modified to hold the environmental chamber and VisiSens secure, and is itself restrained to a table to reduce movement

empirically based on maximum fill level before spilling was observed. Tubes were reused no more than 3 times, and labeled to prevent mixing of solutions (i.e., a tube originally containing media being filled with water).

#### 2.2.4. Oxygen Mass Transfer Measurement

All oxygen mass transfer measurements were carried out with a prototype VisiSens Platetrack OP (PreSens), using VisiSens PlateTrack 96 software. The VisiSens device was mounted within a Modular Incubator Chamber (MIC-101, Embrient Inc, San Diego, CA, USA) custom-modified with a 12-in cylindrical lid extension to fit the device (Figure 2.2D). The VisiSens was secured to the chamber floor with high-strength Velcro adhesive strips. The chamber and device were then mounted on a custom orbital shaker base designed to secure the chamber at high speeds, and strapped down tightly, with a foam ring to secure the device to the wall of the chamber. The orbital shaker itself is mounted and strapped to a table to minimize vibration and movement at high speeds (Figure 2.3). During operation, a digital accelerometer was affixed to the VisiSens to monitor the X/Y/Z-axis accelerations experienced by the device.

Deep wells and conical tubes were prepared with media and water volumes stated above. A single 96 deep well plate is able to be run within the VisiSens during each cycle, and up to six 50mL conical tubes were run per cycle. Filtered caps on the conical tubes were removed before analysis to minimize impediments to air-liquid gas transfer. Imaging of fluorescent oxygen sensors was programmed for every 30 seconds for the duration of the experiment.

Oxygen content percentages were normalized to the initial image (which was normalized to 100%). Once imaging was programmed, the environmental chamber was sealed and nitrogen was flushed into the chamber continuously to purge O<sub>2</sub>. The orbital shaker was activated and set to a level between 0-400 RPM. 500 RPM measurements were not conducted as this exceeded the operational parameters of the shaker under the equipment load. Once oxygen was fully evacuated from the chamber and media and water oxygen values were at steady state, nitrogen flow was stopped and atmospheric air was continuously pulled into the chamber with a house vacuum. The recovery profile was recorded and the experiment concluded when oxygen again reached a steady state (Figure 2.4). All experiments using the VisiSens were performed in triplicate.

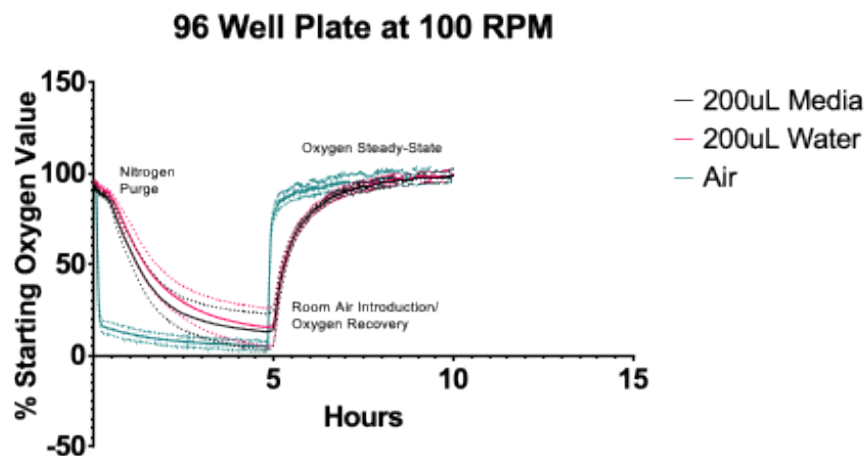


Figure 2.4: Example output of dissolved oxygen concentration in a subset of wells showing the effects of chamber nitrogen purge and room air introduction

### 2.2.5. Oxygen Mass Transfer Analysis

The dynamic method of measuring the oxygen mass transfer coefficient,  $k_L a$ , is used here, facilitated by the removal of dissolved oxygen from the liquid through the nitrogen purge and then re-introduction via ambient air, as shown in Figure 2.4. Such a technique provides two regimes for solution of the equation for the time evolution of the dissolved oxygen concentration, based on the assumption that the dissolved oxygen is well mixed throughout the liquid (i.e. it is constant throughout the liquid):



$$\frac{dC_L}{dt} = \frac{(C^* - C_L)}{\tau_L} \quad (2.1)$$

where  $C_L$  is the dissolved oxygen concentration in the liquid,  $C^*$  is the dissolved oxygen concentration at the gas-liquid interface, and the time constant for the liquid is the inverse of the mass transfer coefficient  $\tau_L = 1/k_L a$ . The concentration at the gas-liquid interface can be calculated using Henry's Law and the concentration of oxygen in the gas  $C_G$ :

$$C^* = HC_G \quad (2.2)$$

where H is Henry's constant for oxygen in water (also represented by  $\alpha$  in later sections), taken to be 0.032. Combining equations 2.1 and 2.2 gives:

$$\frac{dC_L}{dt} = \frac{(HC_G - C_L)}{\tau_L} \quad (2.3)$$

Equation 2.3 can be solved for  $C_L$ :

$$C_L = HC_G(1 - e^{-t/\tau_L}) \quad (2.4)$$

In order to fit to the experimental evolution of oxygen concentration, expressed as a percentage of an initial value which is assumed to be the saturated concentration  $HC_G$ , equation 2.4 is modified to:

$$\frac{C_L}{HC_G} = A(1 - e^{-(t-B)/\tau_L}) \quad (2.5)$$

where  $\frac{C_L}{HC_G}$  is the dissolved oxygen percentage as a decimal,  $A$  is an amplitude correction to allow for situations where the experimental value does not return to 100%, and  $B$  is a time offset to capture the non-zero time at which the ambient air is re-introduced in to the chamber. Fitting  $A, B, \tau_L$  in equation 2.5 to the experimental data allows evaluation of  $k_L a$ .

The above process is commonplace for evaluating  $k_L a$  in shaken containers using the dynamic technique [25]. However, it relies on the assumption that the oxygen concentration in the gas  $C_G$  is constant throughout the process, which may not be the case for applications of the dynamic technique where oxygenated air is first removed then re-introduced in to the chamber. In such a case there may be a time delay in the concentration of oxygen in the air in the immediate vicinity of the air-liquid

interface reaching the value in the supplied air. A simple approach to attempt to account for this delay is described below.

If we consider the time evolution of the concentration of oxygen in the gas  $C_G$  in an analogous way to that of the liquid concentration, we have:

$$\frac{dC_G}{dt} = \frac{(C_\infty - C_G)}{\tau_G} \quad (2.6)$$

where  $C_\infty$  is the oxygen concentration in the chamber air supply. We can solve this as before:

$$C_G = C_\infty(1 - e^{-t/\tau_G}) \quad (2.7)$$

and fit the following to the time evolution measurements in the empty wells/tubes to get a “gas-side” time constant  $\tau_G$ :

$$\frac{C_G}{C_\infty} = A(1 - e^{-(t-B)/\tau_G}) \quad (2.8)$$

The constant value of  $C_G$  in equation 2.3 can now be replaced by the expression in equation 2.7, giving an equation for the time evolution of the dissolved oxygen concentration in the liquid as a function of both the gas and liquid time constants:

$$\frac{dC_L}{dt} = \frac{(C_\infty (1 - e^{-t/\tau_G}) H - C_L)}{\tau_L} \quad (2.9)$$

which can be solved for  $C_L$ :

$$C_L = C_\infty H \left[ 1 - e^{-t/\tau_L} + \frac{\tau_G(e^{-t/\tau_G} - e^{-t/\tau_L})}{\tau_L - \tau_G} \right] \quad (2.10)$$

which can be modified to allow fitting to the experimental data, as before:

$$\frac{C_L}{C_\infty H} = A \left[ 1 - e^{-(t-B)/\tau_L} + \frac{\tau_G(e^{-(t-B)/\tau_G} - e^{-(t-B)/\tau_L})}{\tau_L - \tau_G} \right] \quad (2.11)$$

where  $\tau_G$  is evaluated from fitting equation 2.8 to the experimental data from empty wells/tubes.

We therefore have two methods for evaluating  $k_L a$  from the experimental data: a *standard* method given by fitting data to equation 2.5 and a *bespoke* method given by fitting data to equations 2.8 and 2.11.

### 2.2.6. Interface Evolution Recording and Analysis

Visualization of the air-liquid interface evolution within deep-well and conical tube geometries at different orbital velocities and at different fill volumes was necessary to validate the computational model system and effectively recapitulate experimental conditions. Deep well plates or 50mL TPP tubes were secured tightly to an Extreme Environment orbital shaker (OHAUS, Parsippany, NJ, USA) in an upright configuration. Wells or TPP tubes were filled with basal media or MilliQ water at volumes described in the above sections. The shaker set-up was mounted in front of a HiSpec4 high speed digital camera (FastEC Imaging, San Diego, CA, USA) and recorded at 1000 FPS in static conditions, 100 RPM, 200 RPM, 300 RPM, 400 RPM, and 500 RPM, at constant 19mm throw length on the orbital shaker.

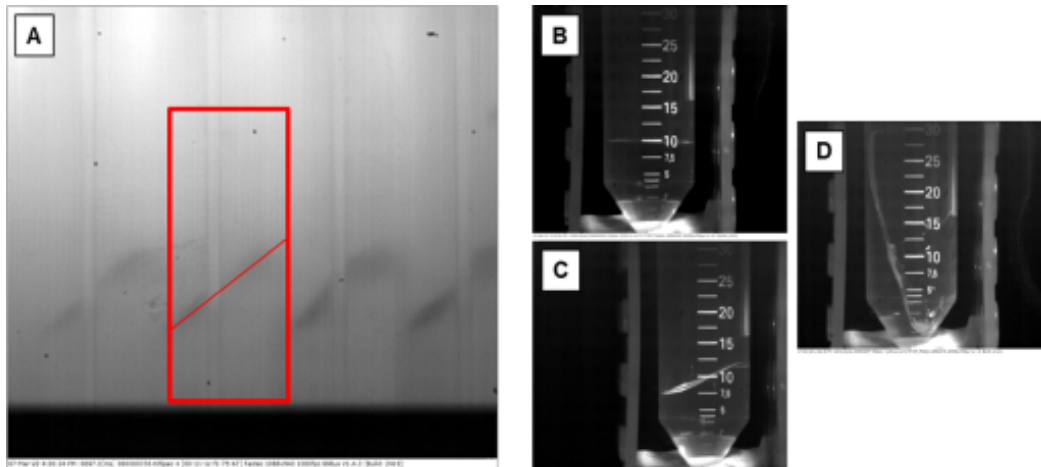
The interface height ( $H_L$ ) was identified from still images (Figure 2.5, A-D) and manually measured via vertical length from the bottom of the air-liquid interface to the top in ImageJ. High speed videos were generated in ImageJ, at a set rate of 60 FPS. All measurements were conducted at least 3 times. Statistical analysis was conducted in GraphPad Prism using an ANOVA with Tukey post hoc testing.

## 2.3. Results

### 2.3.1. Air-Liquid Interface Height

For both water and media evaluated within the deep well plate geometry, interfacial height  $H_L$  did not measurably increase above 0 (initial state) until 300 RPM was reached. At this speed, media  $H_L$  for 200 $\mu$ L, 500 $\mu$ L, and 1000 $\mu$ L fill volumes was  $0.62 \pm 0.19$  mm,  $0.12 \pm 0.07$  mm, and  $0.64 \pm 0.17$  mm, respectively. Media  $H_L$  was significantly lower in the 500 $\mu$ L versus the 1000 $\mu$ L fill volume at 300 RPM ( $P < 0.05$ ). Change in  $H_L$  was significantly different for the 500 $\mu$ L fill volume versus both 200 $\mu$ L and 1000 $\mu$ L for 400 RPM (500 $\mu$ L:  $1.48 \pm 0.28$  mm, 200 $\mu$ L:  $2.66 \pm 0.52$  mm, 1000 $\mu$ L:  $2.22 \pm 0.45$  mm) and 500 RPM (500 $\mu$ L:  $5.75 \pm 0.43$  mm, 200 $\mu$ L:  $4.89 \pm 0.20$  mm, 1000 $\mu$ L:  $4.96 \pm 0.28$  mm) (Figure 2.6A).  $H_L$  for water at these fill volumes followed a similar pattern. At 300 RPM, interfacial height  $H_L$  began to measurably increase, with 200 $\mu$ L, 500 $\mu$ L, and 1000 $\mu$ L  $H_L$  measuring  $1.12 \pm 0.18$  mm,  $1.47 \pm 0.15$  mm, and  $1.30 \pm 0.17$  mm, respectively. Significant variation in interfacial height was only observed at 500 RPM, with both 1000 $\mu$ L ( $6.62 \pm 0.62$  mm) and 500 $\mu$ L ( $6.29 \pm 0.44$  mm) varying significantly versus the 200 $\mu$ L fill volume  $8.46 \pm 0.34$  mm (Figure 2.6B).

Within the 50mL conical tube geometries, interfacial height  $H_L$  was observed to evolve measurably above 0 at 200RPM for both water and media at 10mL and 20mL fill volumes. All conditions exhibited an exponential upward trend with respect to increasing RPM. For media conditions, significant variance in  $H_L$  with respect to fill level was only observed at 500RPM, with 10mL interfacial height measuring  $62.80 \pm 2.86$  mm versus  $77.37 \pm 4.83$  in 20mL ( $p < 0.05$ ) (Figure 2.7C). Water exhibited more variability in interfacial height overall, with significant differences between 10mL and 20mL fill



**Figure 2.5: Representative images from air-liquid interface evolution recordings. A) Red box indicates the outline of a single well within a deep-well plate, with the interfacial height  $H_L$  outlined. Run specifications: 500  $\mu$ L DI water, 500 RPM. B) Conical tube with 10mL media at 100RPM. C) Conical tube at 200 RPM, when an observable change in  $H_L$  becomes visible. D) Conical tube at 500RPM showing large increase in interfacial area.**

volumes beginning at 300RPM. Specifically, the values for 300 RPM for 10mL and 20mL fill volumes were  $25.79 \pm 0.35$  mm and  $30.02 \pm 1.25$  mm, respectively. For 400 RPM, the measured  $H_L$  values were  $41.21 \pm 0.84$  mm and  $46.41 \pm 2.89$  mm and for 500 RPM the values were  $62.53 \pm 2.84$  mm and  $71.89 \pm 2.00$  mm (Figure 2.7D).

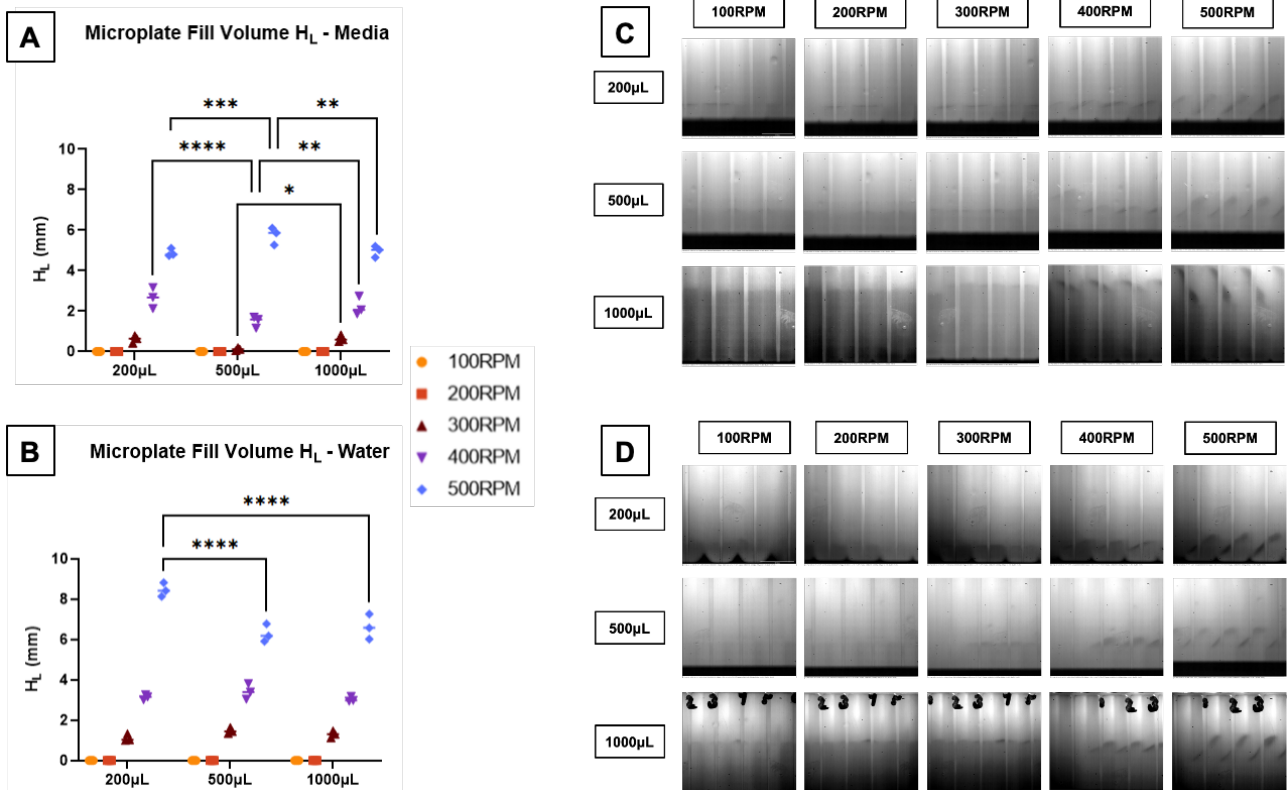
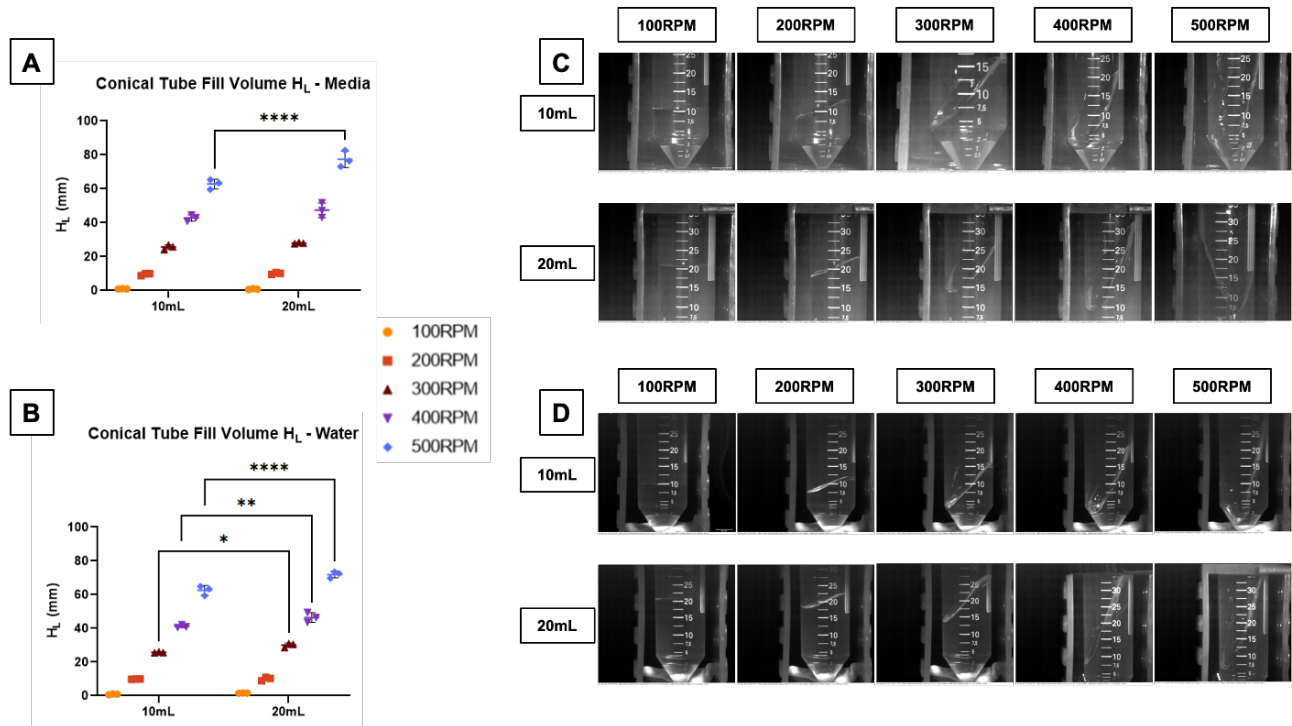


Figure 2.6: Air-liquid interfacial height  $H_L$  data recorded in deep well geometries. Shape/color key denotes RPM value for all plots. A) 96 well plate basal media  $H_L$  at indicated RPMs for fill volumes of 200  $\mu$ L, 500  $\mu$ L, and 1000  $\mu$ L, respectively. B)  $H_L$  data for water at at indicated RPMs for fill volumes of 200  $\mu$ L, 500  $\mu$ L, and 1000  $\mu$ L. C) Still images from 1000FPS recordings of interfacial evolution at varying speeds for media, showing fill volumes of 200  $\mu$ L, 500  $\mu$ L, and 1000  $\mu$ L at 100-500 RPM. D) Still images from 1000FPS recordings of interfacial evolution at varying speeds for media. For C & D, Scale bars (200  $\mu$ L/100RPM image) are equal to 10mm. N=3, all groups. \* =  $P < 0.05$ , \*\* =  $P < 0.01$ , \*\*\* =  $P < 0.001$ , \*\*\*\* =  $P < 0.0001$ .



**Figure 2.7: Air-liquid interfacial height  $H_L$  data recorded in deep well geometries. Shape/color key denotes RPM value for all plots. A) Media  $H_L$  for conical tubes, with fill volumes of 10mL and 20mL, at indicated RPM. B) Water  $H_L$  for conical tubes, with fill volumes of 10mL and 20mL, at indicated RPM. D) Water  $H_L$  for conical tubes, with fill volumes of 10mL and 20mL, at indicated RPM. C) Still images from 1000FPS recordings of interfacial evolution at varying speeds for media, showing fill volumes of 200  $\mu$ L, 500  $\mu$ L, and 1000  $\mu$ L at 100-500 RPM. D) Still images from 1000FPS recordings of interfacial evolution at varying speeds for media. For C & D, Scale bars (200  $\mu$ L/100RPM image) are equal to 10mm. N=3, all groups. \* = P<0.05, \*\* = P<0.01, \*\*\* = P<0.001, \*\*\*\* = P<0.0001.**

### 2.3.2. Oxygen Mass Transfer Coefficients

For well plate data both standard and bespoke fitting methods were used. Table 2.1 below shows the evaluated  $k_L a$  values for all combinations of RPM and well fill volume and fill liquid for both methods.

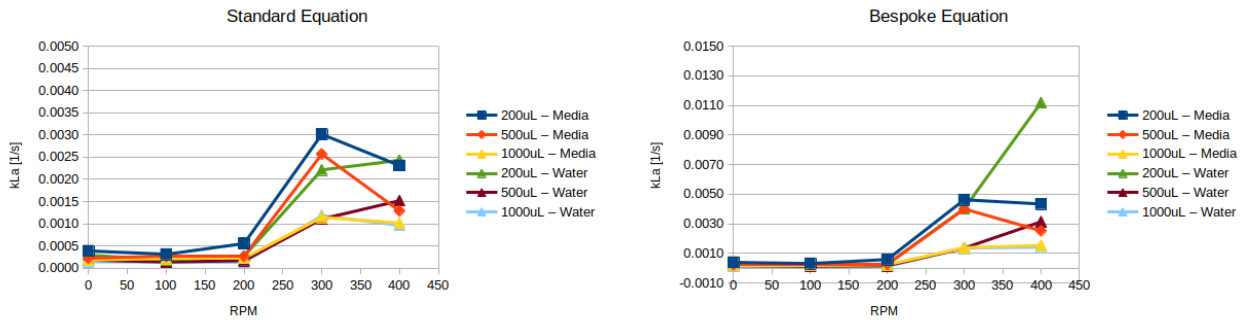
Fit	RPM	200uL – Media	500uL – Media	1000uL – Media	200uL – Water	500uL – Water	1000uL – Water
Standard	0	0.00039	0.00023	0.00018	0.00029	0.00018	0.00015
Standard	100	0.00032	0.00027	0.00022	0.00019	0.00014	0.00014
Standard	200	0.00056	0.00026	0.00023	0.00027	0.00017	0.00014
Standard	300	0.00302	0.00257	0.00115	0.00221	0.00111	0.00118
Standard	400	0.00231	0.00129	0.00102	0.00243	0.00152	0.00097
Bespoke	0	0.00040	0.00023	0.00018	0.00029	0.00018	0.00015
Bespoke	100	0.00032	0.00027	0.00022	0.00019	0.00014	0.00014
Bespoke	200	0.00059	0.00027	0.00024	0.00027	0.00017	0.00014
Bespoke	300	0.00462	0.00400	0.00139	0.00403	0.00136	0.00136
Bespoke	400	0.00434	0.00252	0.00155	0.01119	0.00314	0.00142

**Table 2.1: Oxygen transfer coefficient values for all combinations and both methods for 96 well-plates, averaged across all wells and all repeats for each combination.**

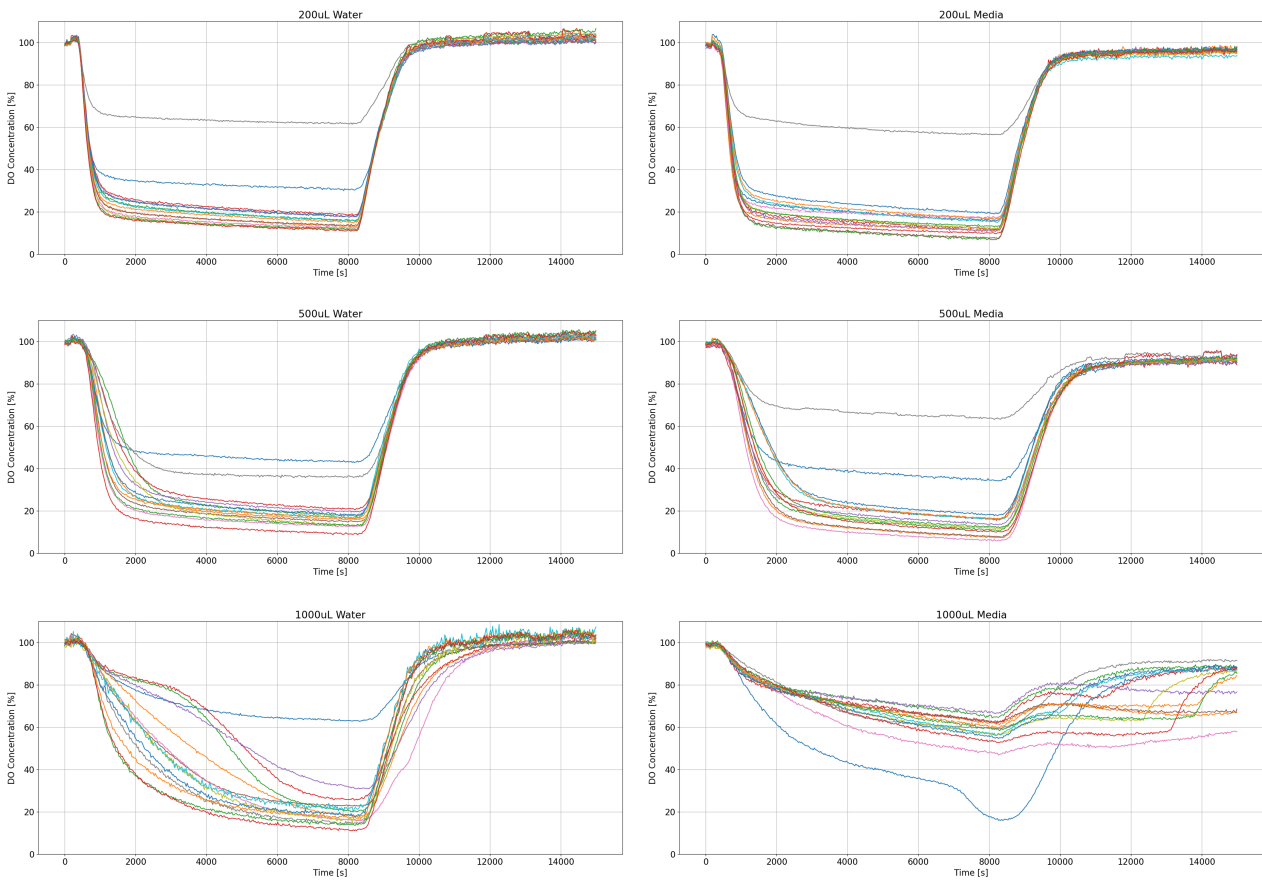
The data from Table 2.1 is visualised in Figure 2.8 below. It is clear from the figure that there is an increasing trend in  $k_L a$  values up to 300 RPM and a drop at 400 RPM. There was a significant degree of variability across both repeat runs at the same RPM and across wells with the same fill volume and fill liquid within a single run. This variability was most significant at 400 RPM. Figure 2.9 shows the

measured data for one 400 RPM run, with each graph grouped by fill volume and fill liquid. The variability within each group and across groups is evident.

Due to the variability in the well plate data, and the differences in  $k_L a$  values between the standard and bespoke methods (the latter of which is a considerable simplification of the transport of air into the wells), the values from the two methods are considered to be lower and upper bounds of what may be expected, and will be compared to other results on this basis.



**Figure 2.8: Graphs of oxygen transfer coefficient data from Table 2.1.**

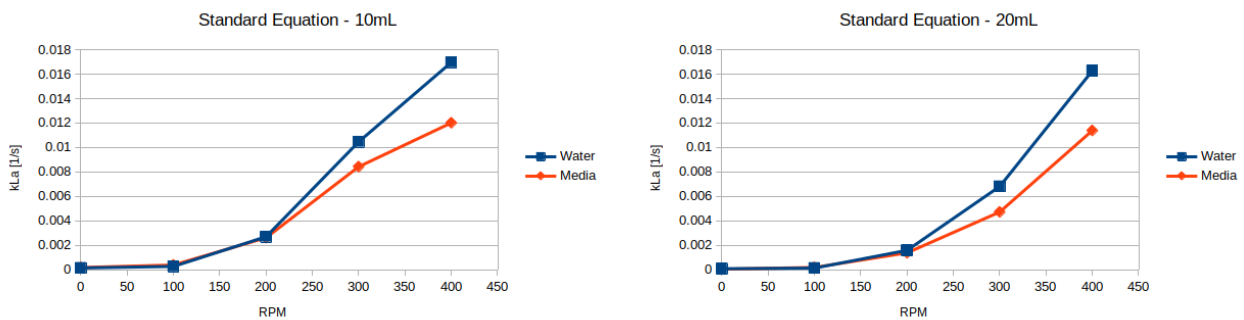


**Figure 2.9: Graphs of oxygen concentration measured values for a 400 RPM run grouped by well fill volume and liquid.**

For the TPP tube evaluation, only the standard method was applied due to the removal of the tube caps allowing a sufficiently fast transport of supplied air in to the tubes for the gas-side timescale to be considered negligible. Table 2.2 gives the calculated values of the mass transfer coefficient across the range of parameters considered, which are visualised in Figure 2.10.

RPM	10mL – Media	20mL – Media	10mL – Water	20mL – Water
0	0.00019	0.00006	0.00016	0.00009
100	0.00040	0.00020	0.00028	0.00015
200	0.00263	0.00139	0.00271	0.00160
300	0.00843	0.00473	0.01047	0.00682
400	0.01202	0.01139	0.01697	0.01628

**Table 2.2: Oxygen transfer coefficient values for all combinations and both methods for TPP tubes, averaged across all tubes and all repeats for each combination.**

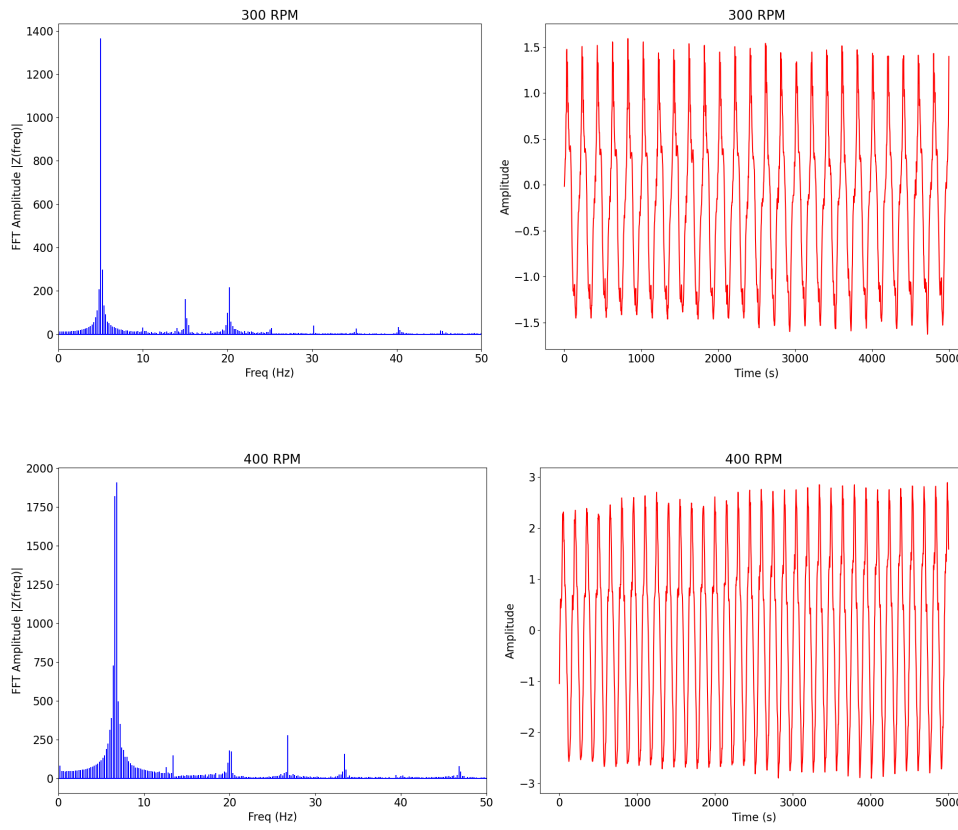


**Figure 2.10: Graphs of oxygen transfer coefficient data from Table 2.2.**

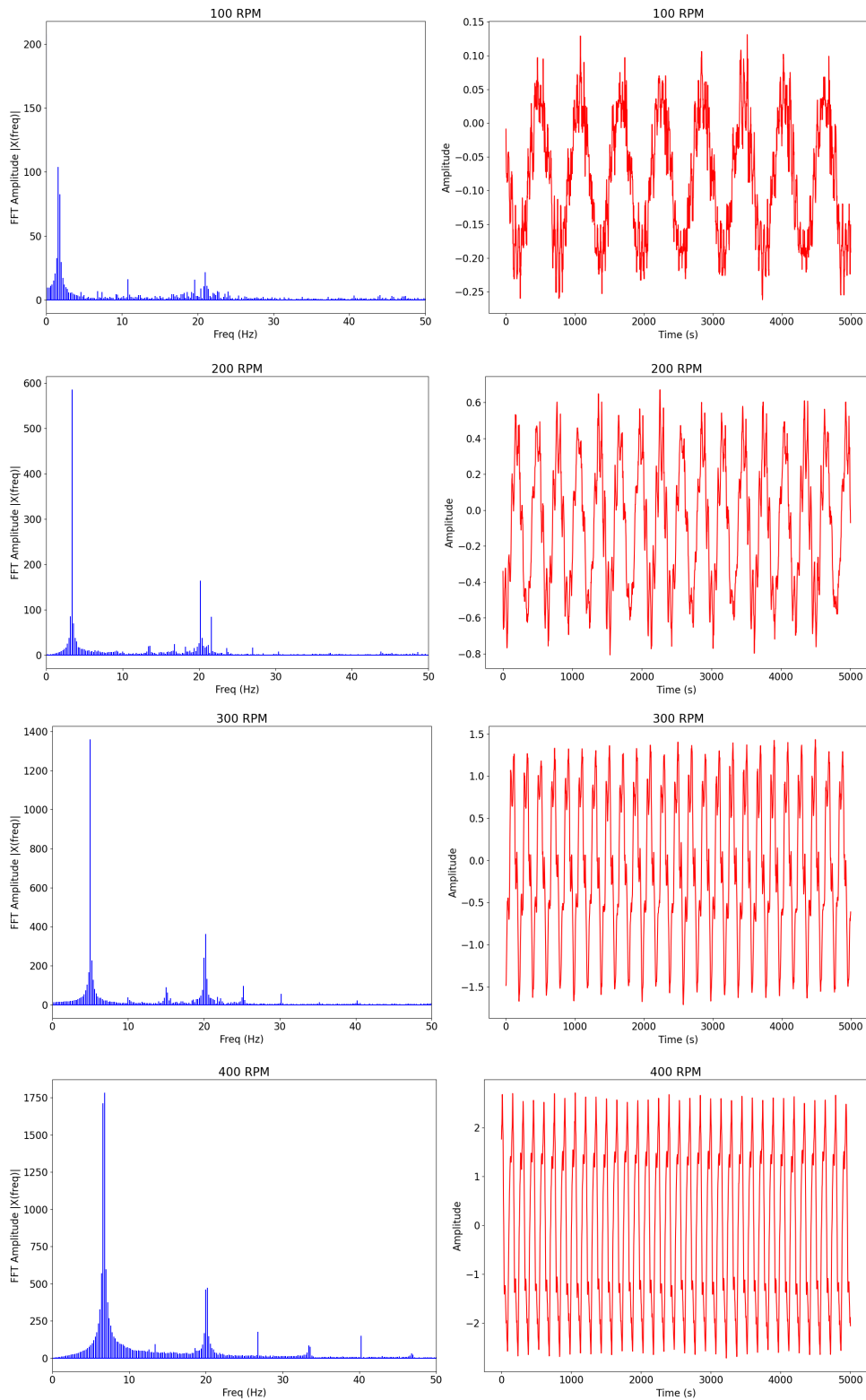
### 2.3.3. Shaking Table Acceleration

The accelerations from the accelerometer were processed to show the amplitude of acceleration in the x-direction (one of the directions in the plane of the shaking table motion). A fast Fourier transform using the numpy python module (numpy.fft) was used to extract the dominant frequencies of the motion. Figures 2.11 and 2.12 plot the results of the transform and the acceleration amplitudes as a function of time for runs with well plates and TPP tubes respectively. It is clear that in addition to the primary frequency associated with the RPM applied there are other frequencies resulting from the overall vibration of the shaking table and chamber. An additional 20Hz vibration is consistently experienced across both well plates and TPP tubes.





**Figure 2.11: Graphs of frequency (left column) and amplitude (right column) from accelerometer data for 96 wells at 300 and 400 RPM.**



**Figure 2.12: Graphs of frequency (left column) and amplitude (right column) from accelerometer data for TPP tubes at 100 to 400 RPM.**

## 2.4. Analysis & Discussion

### 2.4.1. Interface Height

Change in air-liquid interfacial area plays a critical role in evolution of  $k_La$  and oxygen transport within a bioreactor environment [2, 3]. Consequently, a firm understanding of how our model systems could predict and recapitulate experimentally-observed values was critical.

With respect to cell viability and oxygen consumption, increasing interfacial area to permit gas transport while minimizing shear stress due to fluid flow is critical. It is well-established that shear forces can induce phenotypic changes to cells, trigger apoptosis, or physically damage them at high speeds [4–6]. For cellular agriculture applications, this is particularly pertinent: maintenance of cell viability, proliferation, and cell state within a bioreactor are critical process considerations that must be well-controlled.

Fill volume appeared to have a significant effect on  $H_L$ . Within deep-well plates, significant variation in  $H_L$  between 200 $\mu$ L, 500 $\mu$ L and 1000 $\mu$ L fill volumes was observed beginning at 500 RPM for water, but at 300 RPM for media, with media exhibiting more variance, potentially due to the presence of various solutes modifying fluid properties. However, for conical tubes, this pattern was reversed, and with a significant increase in average  $H_L$  for water observed for the 20mL fill volume versus 10mL, at 300 RPM. An  $H_L$  increase from the 10mL to the 20mL fill volume was only observed at 500 RPM for media. This may be due to differences in aqueous affinity between the plastics comprising the well plates and tubes.

With respect to the experimental geometries employed in this study,  $H_L$  increased non-linearly with respect to orbital velocity. For deep-well plates, we observed for both water and basal media that a measurable increase in  $H_L$  was observed at 300 RPM, which was observed consistently across all fill volumes. The necessary velocity to increase interfacial area was lower for 50mL conical tubes (200 RPM). This is likely due in part to the larger water volume evaluated, but may again be due partly to differences in aqueous affinity between the well plates and tubes. This lower velocity may make the conical tube system a more effective scaled-down bioreactor model with respect to cell survival. It should also be noted that we only measured discrete RPM values in increments of 100 RPM - the true lower threshold to increase interfacial area most likely falls between values, and future experiments should evaluate a more continuous series of velocities to determine this definitively.

### 2.4.2. Oxygen Transport Rate Measurements

The  $k_La$  values measured experimentally varied significantly with respect to orbital velocity and fill volume, trending in a similar pattern to the interfacial area measurements. Conical tube tests exhibited faster oxygen recovery than deep-well plates, despite having greater volume, supporting the idea that surface area plays a crucial factor in determining oxygen transport.

It should be noted that well-to-well and tube-to-tube variability in experiments was often high, and due to this some oxygen traces during the nitrogen purge phase appear to never reach zero despite reaching plateau. We found that variability appeared to be consistent with specific regions the well plate and conical tube holder across experiments, and therefore consider that the variability was due in part by issues with the provided fluorescence monitoring and analysis software. Future iterations of this project should ideally work to refine this data collection method to increase consistency and accuracy of oxygen transport values.

Figures 2.13 and 2.14 below compare the well plate  $k_L a$  and interface height data to the published data from [10] which considered 96 well plates of smaller ( $\approx 6.6\text{mm}$ ) diameter at a range of RPMs, filled to  $200\mu\text{L}$  with a solution comprised of different substances to enable a chemical method of determining  $k_L a$ . Figure 2.13 shows that the behaviour at low RPM is consistent across the two datasets, and the increase from the zero RPM level of  $k_L a$  is in good agreement with regards the agitation radius. The difference may well be due to the well diameter difference, or the unknown values of surface tension in the media from the published data [10]. The significant difference in the zero RPM value of  $k_L a$  is worthy of further comment. Without agitation, the dissolved oxygen concentration in the liquid will not be well mixed, with only diffusion providing transport in the vertical direction from the gas-liquid interface to the bottom of the well. As a result, equation 2.1 is not well suited to describe the evolution of a uniform concentration. This assumption of a well mixed condition, along with the possibility of the chemical method for evaluating  $k_L a$  being analogous to having a sensor at the gas-liquid interface, as opposed to at the bottom of the well as in the current work, are potential reasons for the zero RPM value difference.

Figure 2.14 makes a similar comparison for the interface height, showing good agreement to the data in [10] for the RPM at which the interface height begins to increase significantly. The plot for the current work, with a shaking radius of  $a = 0.0095$  m falls between the plots from published data for  $a = 0.00625$  m and  $a = 0.0125$  m, as expected.

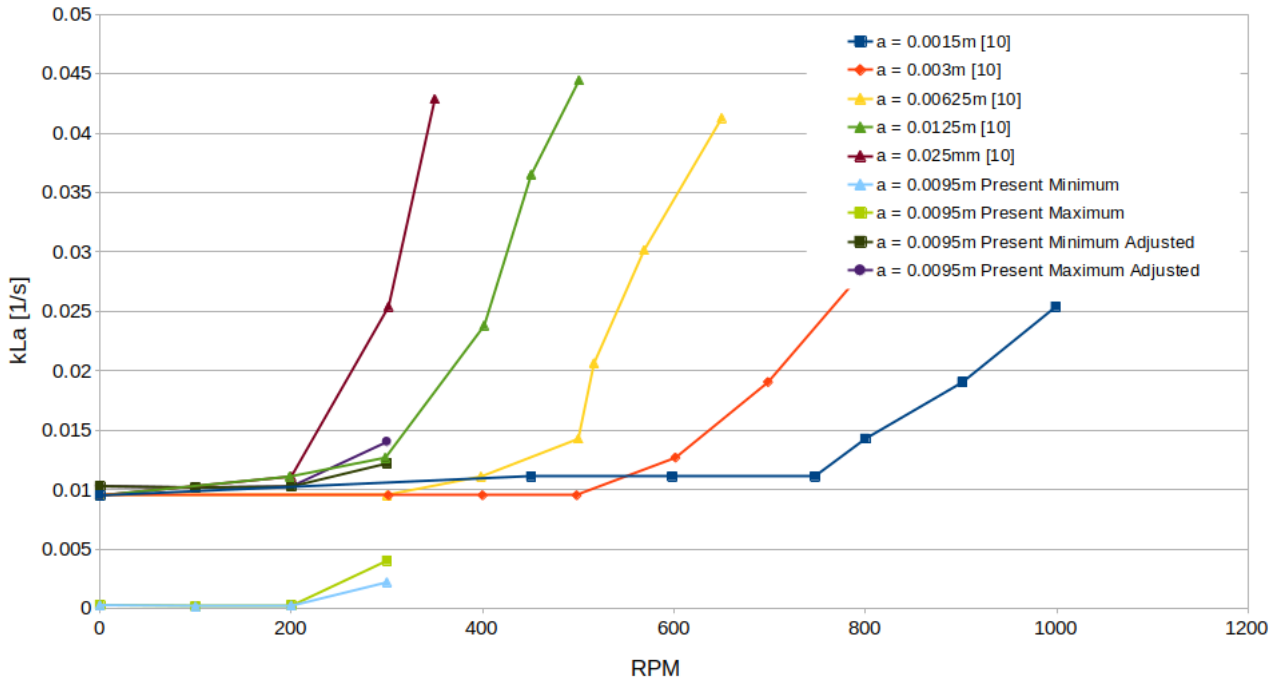


Figure 2.13: Comparison of  $k_L a$  data from the present work to that published in [10], where  $a$  is the agitation radius of the shaking table. Present data limited to 300 RPM. Present minimum and maximum refer to values from the standard and bespoke methodologies respectively. Adjusted data has the zero RPM value of published data [10] added (approx. 0.01).

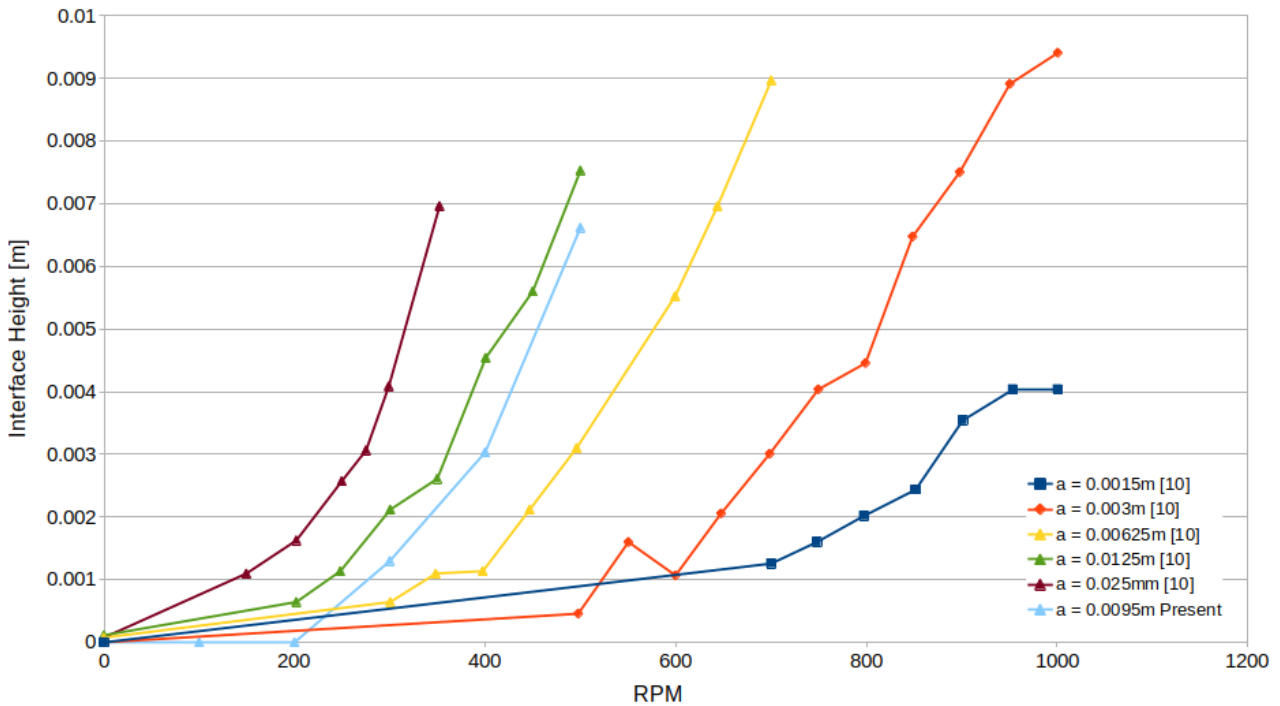


Figure 2.14: Comparison of  $H_L$  data from the present work to that published in [10], where  $a$  is the agitation radius of the shaking table. Present data limited to 300 RPM.

## 2.5. Conclusions & Recommendations

Overall, the scaled-down experimental system represents a viable method to test various bioreactor operational parameters in a high-throughput, low-cost format, with fluorescent oxygen sensing providing real-time feedback on media oxygenation and cellular respiration. Future iterations of this system should investigate cell oxygen uptake and metabolism directly, and evaluate the impact of environmental variables including varying the throw length of the orbital shaker and the impact of different temperatures and humidity on oxygen transport within this system.

The prototype PreSens VisiSens system and SF-RPSu4 oxygen sensor foils provided an effective tool to evaluate real-time changes in oxygen content in air, water, and media. The device was used almost daily for over a year and put under orbital velocities of up to 500 RPM, and continued to function effectively. The provided software, although still in a prototype state, is easy to use after training and stores data automatically over the course of an experimental run. The oxygenation data the device recorded was consistent and effectively supported generation of the computational models. However, it possesses several limitations that must be noted, and considerations for future use that should be addressed. The device does not operate effectively at 37° centigrade, rendering its use in a cell culture incubator nonviable. When incubator runs were attempted, the connection between the VisiSens and the external laptop fails. If this device is used for cell culture experiments going forward, this error must be addressed.

As stated previously, we observed high sample-to-sample variability across multiple experiments, often in the same locations on the 96-well plate or tube holder, and in some instances, wells would not register as functional/detectable in the software. While a software patch from PreSens resolved the latter issue, the former should be assessed before moving into live cell experiments, which will likely have greater variability in oxygenation over time and could be skewed by software detection issues.

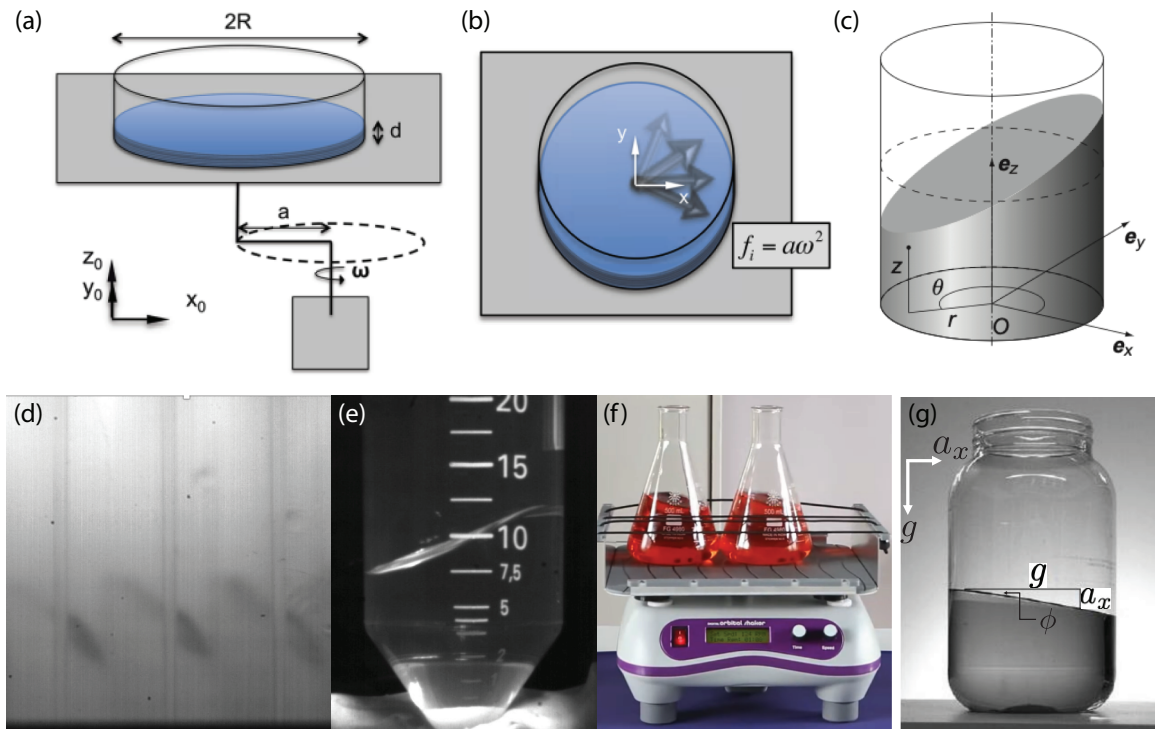
Subsequent work could consider activities to reduce the sample-to-sample variability, such as performance analysis and development of the air flow within the chamber to remove any induced variability from this source.

Another area for further consideration could be the effects of the additional vibrations experienced by the shaking table system as a whole on the mass transfer performance. With the measurements made here it is possible to include this as input in to modelling activities.

### 3. Reduced Order Modeling

#### 3.1. Overview

The goal of this portion of the work is to develop and validate a simple mathematical model that can be solved efficiently to predict certain features of the fluid response associated with orbital shaking of cylindrical containers. This is accomplished by identifying the dominant physics of the problem and making many necessary simplifications, which are explained throughout.



**Figure 3.1:** (a) Schematic of orbital shaking of a cylindrical fluid vessel [7]. (b) Top view of container, showing equivalent inertial forcing with magnitude  $a\omega^2$  that rotates with the orbital frequency [7]. (c) In the quasi-static limit, the free surface takes the shape of a tilted plane [8]. (d-f) Observations of interface shape across scales: (d) Deep wells (500 RPM, 500  $\mu\text{L}$  fill volume), (e) TPP tubes (200 RPM, 10 mL fill volume), and (f) flasks (Image Credit: Heathrow Scientific). (g) The free surface of a fluid undergoing a uniform steady lateral acceleration  $a_x$  in a gravitational field  $g$  takes the form of a tilted plane (Image Credit: Metin Guner).

As shown in Figure 3.1(a), a cylindrical vessel of radius  $R$  filled to a depth  $d$  is agitated with orbital radius  $a$  and angular frequency  $\omega$ . The orbital frequency  $f$  in rotations/second (Hertz) is related to  $\omega$  via  $\omega = 2\pi f$ . In the non-inertial reference frame moving with the container, the orbital agitation can be equivalently represented as a steadily rotating inertial body forcing of magnitude  $a_x = a\omega^2$  (Figure 3.1(b)). Note that the frame of reference moves rectilinearly along a circular trajectory, which is distinct from moving into a rotating reference frame, and thus no other fictitious forces need to be included. As in prior work [7], we define a non-dimensional forcing strength  $F = a\omega^2/g$  that describes the relative strength of the forcing (lateral) to gravity (downward). If the body forcing is not rotating (and contact line effects can be neglected) the interface takes the form of a static tilted plane that intersects the cylindrical container as shown in Figure 3.1(c). As imaged in Figures 3.1(d-f), similar planar-like interfaces are observed in the dynamic experiments performed by us for well plates and

TPP tubes, as well as larger geometries such as flasks in other experiments. In each case, the perturbed surface steadily rotates with orbital frequency.

## 3.2. Modeling

### 3.2.1. Potential Flow Model

As derived in prior work [7,9] under the assumptions of potential flow (inviscid, irrotational flow), an exact solution can be found for the interface height  $\eta(r, \theta, t)$ :

$$\eta(r, \theta, t) = \frac{a\omega^2}{g} \cos(\omega t - \theta) \left[ r + \sum_{n=1}^{\infty} \frac{2R}{(\epsilon_{1n}^2 - 1)} \frac{\omega^2}{(\omega_{1n}^2 - \omega^2)} \frac{J_1(k_{1n}r)}{J_1(\epsilon_{1n})} \right] \quad (3.1)$$

where  $\omega_{1n}$  is the  $n^{\text{th}}$  resonant wave frequency of the container and is defined by the dispersion relation of gravity-capillary waves

$$\omega_{1n}^2 = \left( gk_{1n} + \frac{\sigma k_{1n}^3}{\rho} \right) \tanh k_{1n}d \quad (3.2)$$

where  $\sigma$  and  $\rho$  are the surface tension and density of the fluid, respectively. Prior works only considered the gravitational component [7,9], however due to the small scales of interest surface tension has also been included in this formulation for the present work.

Furthermore,  $k_{1n} = \epsilon_{1n}/R$ , and  $\epsilon_{1n}$  is the  $n^{\text{th}}$  root of  $J_1'(s)$ . The value of  $\epsilon_{1n}$  for the first five wave modes is 1.841, 5.331, 8.536, 11.706, and 14.864. While this solution is exact, it neglects the effects of fluid viscosity and does not enforce any contact angle at the boundaries of the container. This model will be referred to throughout as the *potential flow* model.

### 3.2.2. Quasi-static Model

When dynamic effects are negligible, a quasi-static approximation is often valuable towards further simplifying the governing equations. In such a limit, the change of the forcing is sufficiently slow that at each moment in time the fluid has time to respond as if it were in an instantaneous static equilibrium. For the current problem of interest, this is satisfied when the the orbital frequency  $\omega$  is much slower than the first resonant wave mode of the geometry  $\omega_{11}$ . By taking the limit of equation 3.1 when  $\omega \ll \omega_{11}$  we find the following interface shape:

$$\lim_{\omega \ll \omega_{11}} \eta(r, \theta, t) = \frac{a\omega^2}{g} \cos(\omega t - \theta)r. \quad (3.3)$$

Thus in this quasi-static limit, the surface shape can be expressed as



$$\eta_{qs}(r, \theta, t) = F \cos(\omega t - \theta)r \quad (3.4)$$

This corresponds to the tilted plane depicted in Figure 3.1(g) under a constant lateral forcing  $a_x = Fg$ , and steadily rotating with the orbital frequency  $\omega$ . This model carries the same assumptions as the full potential flow model, but with the additional quasi-static criterion  $\omega \ll \omega_{11}$ . Note that the value of  $\omega_{11}$  decreases with  $R$ , and thus the quasi-static model is expected to remain a better approximation for small scale vessels. For a given container shape and set of fluid properties, the shape of the interface is determined by the single non-dimensional parameter  $F$ . The angular tilt  $\phi$  of the surface relative to the horizontal can be directly written as

$$\phi = \tan^{-1} F \quad (3.5)$$

the interfacial area  $A$  as

$$A = \pi R^2 \sqrt{F^2 + 1} \quad (3.6)$$

and the maximum height difference  $h_L$  over the interface as

$$h_L = 2RF. \quad (3.7)$$

This model will be referred to throughout as the *quasi-static* model.

### 3.2.3. Young-Laplace Model

The prior models have ignored the effect of contact angle (solid wettability), which is anticipated to be important at small scales. However a full analytical solution of the form of equation 3.1 that also satisfies the contact angle condition at the walls of the container does not exist. However if we again restrict ourselves to the quasi-static limit, a model for the interface shape that does allow for specification of a contact angle (in the form of a boundary condition) is the Young-Laplace equation:

$$\rho g \eta_{YL} + \rho F g x = \sigma \nabla \cdot \hat{n} \quad (3.8)$$

where  $\hat{n}$  is the unit vector normal to the interface. The divergence of the normal vector ( $\nabla \cdot \hat{n}$ ) can be expressed using standard vector calculus identities and is a function of the spatial derivatives of  $\eta_{YL}$ . If the contribution from surface curvature is neglected ( $\sigma = 0$ ), the prior planar quasi-static solution is recovered (but by dropping the derivatives, no boundary conditions can be enforced). Equation 3.8 is a nonlinear partial differential equation (PDE) in two spatial dimensions. The contact angle  $\theta_c$  enters in the boundary condition to this PDE:

$$\underline{\nabla}\eta_{YL} \cdot \hat{r} \Big|_{r=R} = \tan \left( \frac{\pi}{2} - \theta_c \right). \quad (3.9)$$

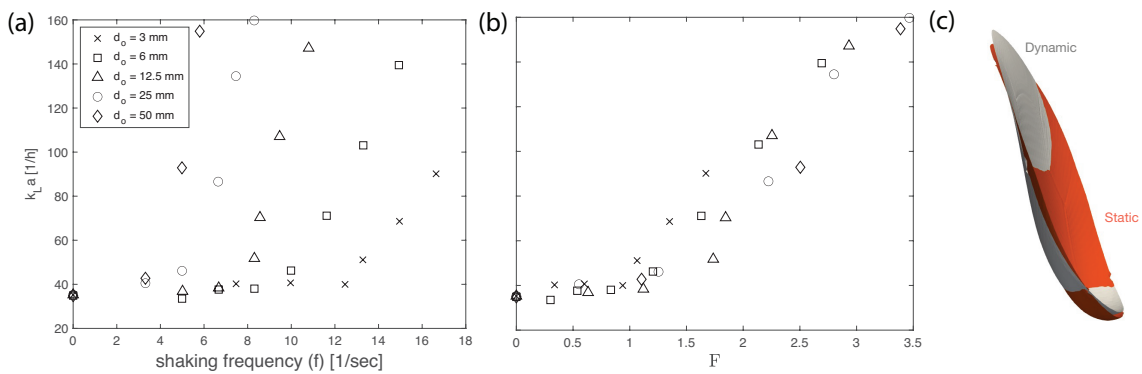
While these equations must be solved numerically in general, they are rather efficient to compute, taking only a few seconds on a standard laptop or desktop computer. For a given well radius and set of fluid properties, the solution now depends on both  $F$  and  $\theta_c$ .

In the present work, these equations are solved using the built-in MATLAB function 'pdenonlin' on a discretized circular domain. Henceforth, this model will be referred to as the *Young-Laplace* model, although it also relies on a quasi-static assumption.

### 3.3. Results

#### 3.3.1. Comparison to Prior Literature

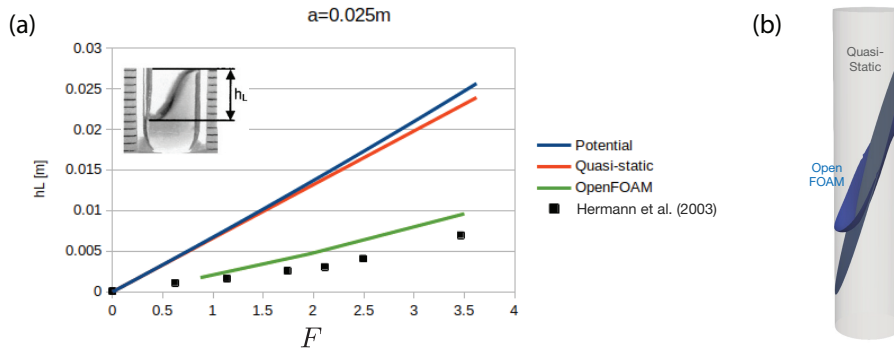
As a first test of our model and assumptions, we turn to the preceding experimental work of Hermann et al. [10] who studied the fluid motion and oxygen transfer on orbitally shaken deep well plates. Their  $k_L a$  data is re-plotted in Figure 3.2(a), and shows clear dependence on both orbital diameter ( $d_0 = 2a$ ) and frequency. When the same data is plotted with the forcing parameter  $F$  on the abscissa in Figure 3.2(b), the data collapses nearly along a single curve. This finding suggests that  $a$  and  $\omega$  are not particularly meaningful as independent control parameters in this case, but rather their combination as defined in the single parameter  $F$  is sufficient to capture the system behavior (as suggested by the quasi-static theories). Additionally, OpenFOAM simulations were performed (resolving the complete time-dependent 3D fluid motion and interface dynamics) and good agreement was found between both dynamic and static simulations for some representative cases as shown in Figure 3.2(c). This agreement directly implies that the quasi-static assumption is valid, in those cases.



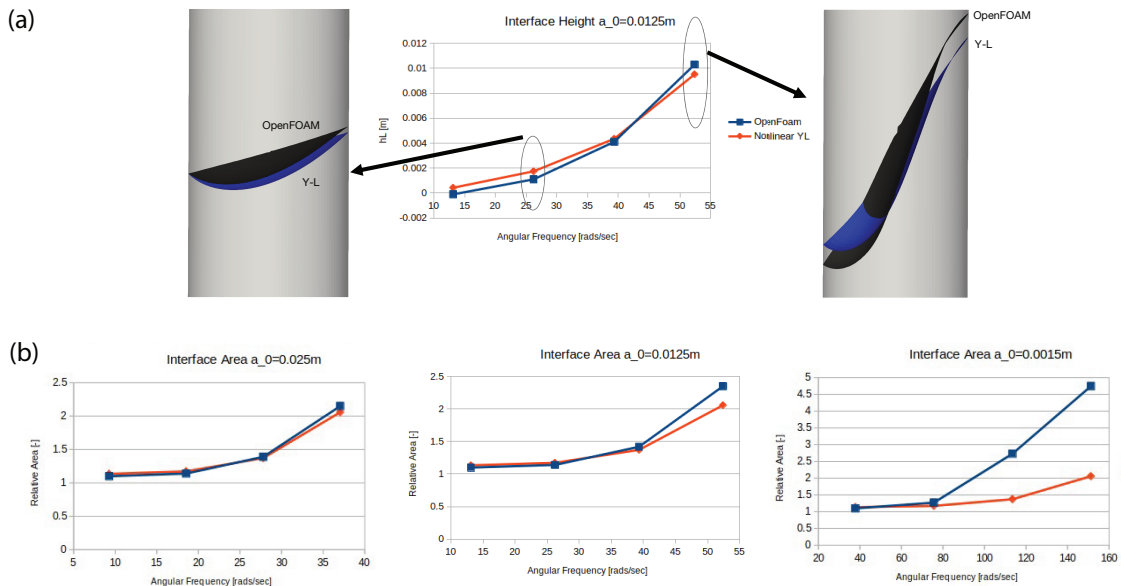
**Figure 3.2: (a) Data on  $k_L a$  from [10] shown as a function of frequency for several orbital diameters. (b) The same data collapses approximately along a single curve when plotted again the non-dimensional forcing parameter  $F$ . (c) Prediction of the interface shape in a deep well case of [10] from OpenFOAM simulations for an equivalent dynamic ( $a = 0.0125m$ ,  $F = 3.5$ ) and static ( $a_x = 3.5g$ ) simulation showing good agreement, lending support to the quasi-static assumption.**

We make direct comparison between the measured rise height and that predicted by the potential flow and quasi-static models in Figure 3.3(a), and see that the both models significantly overpredict the overall surface deformation. Nevertheless, the potential flow and quasi-static models show similar

predictions to each other for this case, suggesting dynamic effects are not playing a pronounced role for these parameters. The OpenFOAM results however show good agreement with the experimental measurements. When comparing the predicted interface shape in more detail to the equivalent prediction of the OpenFOAM simulation (Figure 3.3(b)), it is evident that at least some of the discrepancy lies in the fact that the quasi-static model is unable enforce the correct contact angle, highly relevant at these small scales, as the meniscus is comparable to the size of the geometry.



**Figure 3.3: (a) Comparison of rise height  $H_L$  between experiments of [10], potential flow model, quasi-static model, and OpenFOAM simulations. The reduced order models (potential flow and quasi-static) significantly overpredict the rise height due to their failure to include the correct contact angle. (b) Comparison of interface shape between quasi-static and OpenFOAM models. The Young-Laplace model is proposed to resolve this discrepancy.**



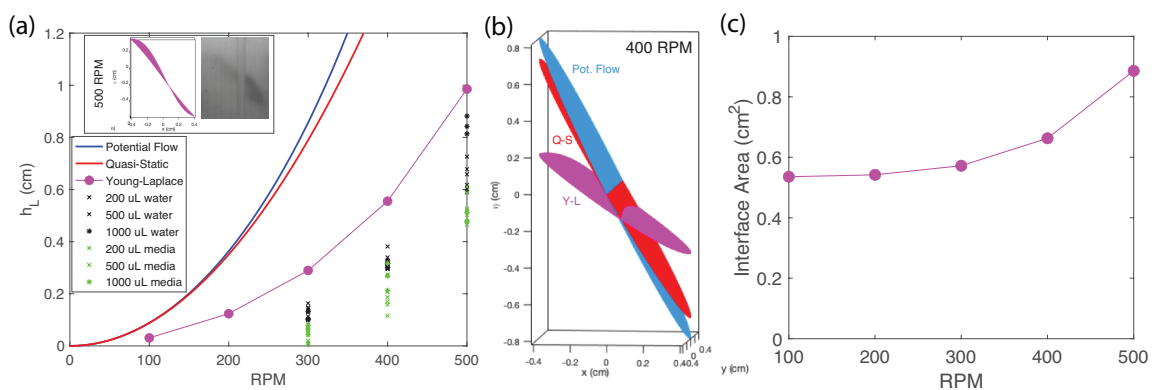
**Figure 3.4: (a) Comparison of rise height  $H_L$  between OpenFOAM simulation and Young-Laplace model for  $a = 0.0125$  m for parameters of [10]. Direct comparisons of complete interface shapes are shown for two agitation frequencies. The enforcement of the correct contact angle in the Young-Laplace model dramatically reduces the predicted height difference as compared to the simpler quasi-static model. (b) Interfacial area (relative to cylinder cross-section) for the OpenFOAM simulations and Young-Laplace model at three different agitation radius. At higher frequencies, the model predictions diverge, indicating the anticipated breakdown of the quasi-static assumption.**

The comparison improves substantially when the contact angle is correctly enforced via the Young-Laplace model, as demonstrated in the comparison in Figure 3.4(a). Predictions for the interfacial area are shown in Figure 3.4(b) for three agitation radii, with good agreement when  $\omega \lesssim 55$  rad/s (525 RPM). For the parameters considered here, the first wave resonance is estimated at  $\omega_{11} = 134$  rad/s (1280 RPM) and it is suspected that the discrepancy at higher frequencies is caused by the neglect of dynamic (wave) effects in the Young-Laplace model. This hypothesis could be further tested in the future with additional OpenFOAM simulations where both the dynamic and static cases are simulated for more cases.

### 3.3.2. Well Plate Predictions

Next we make comparison between our deep well plate experiments and the predictions of the three reduced order models in Figure 3.5(a). Consistent with the comparison made in the prior section for existing well plate data, the potential flow and quasi-static models significantly overpredict the observed free surface height difference and are thus not useful models for this geometry. Note that the potential flow and quasi-static models once again do not differ significantly from one another, suggesting dynamic effects only play a minor role. For this case,  $\omega_{11} = 989$  RPM, and orbital frequencies only up to 500 RPM are investigated.

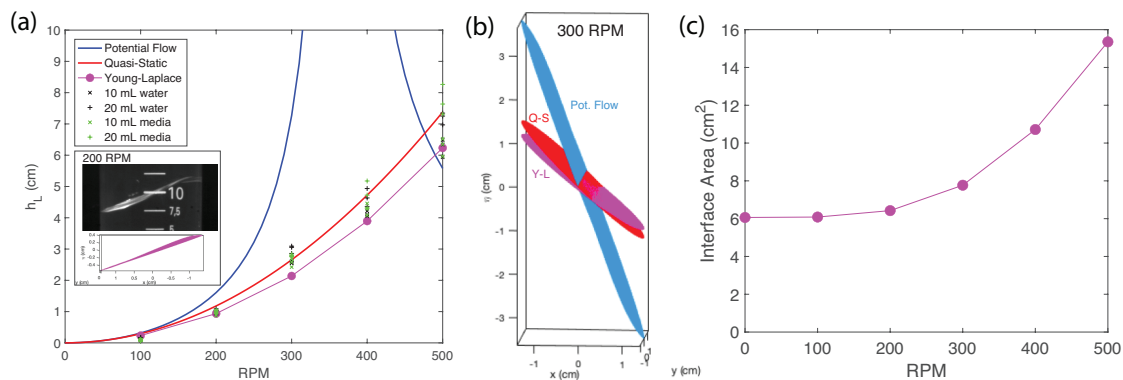
However, the Young-Laplace does a much better job at predicting the measured surface displacements by enforcing the correct contact angle at the walls. There is still some modest overprediction as compared to experiment, which could be related to other effects neglected in the model such as viscosity or contact line friction or hysteresis, or possible uncertainties in the experiment due to the translucent side walls. The predicted interface shapes from the three models are shown in Figure 3.5(b) for 400 RPM: the potential flow and quasi-static profiles are similar (irrelevance of dynamic effects), whereas the predicted deformations from the Young-Laplace model are smaller (suggesting importance of contact angle and meniscus effects). Figure 3.5(c) shows the predicted interfacial area from the Young-Laplace model. Significant increases in area are only predicted above 300 RPM.



**Figure 3.5: Well plate predictions. (a) Comparison of rise height  $H_L$  between experiments and models for the deep well plate case. The inset shows a comparison between an experimental image and the predicted interface (Young-Laplace) at 500 RPM. (b) Predictions of interface shape from the three models for 400 RPM. (c) Interfacial area prediction from Young-Laplace model.**

### 3.3.3. TPP Tube Predictions

Finally, we make comparison between the TPP tube experiments and the three models in Figure 3.6(a). In this case, the quasi-static and Young-Laplace models differ only slightly. This similarity is anticipated due to the larger scales of the container, with the meniscus taking up a smaller fraction of the radii. Both models predict the measured rise height very well. For these parameters,  $\omega_{11} = 366$  RPM, and thus it was anticipated that dynamic wave effects may play a role for the TPP tubes. This resonant phenomenon is associated with the predicted divergence of surface height in the potential flow model at  $\omega_{11}$ . Somewhat surprisingly, this dramatically enhanced dynamic response is not observed in the experimental measurements. Damping effects have been completely ignored in the present model (viscosity, contact line friction) and could conceivably be playing an important role in attenuating the dynamic fluid response. Further modeling work is needed to elucidate such effects. The predicted interface shapes from the three models are shown in Figure 3.6(b) for 300 RPM: the quasi-static and Young-Laplace profiles are similar for this case (suggesting less relevance of contact angle and meniscus effects for this larger geometry). Figure 3.6(c) shows the predicted interfacial area from the Young-Laplace model. Significant increases in area are only predicted above 200 RPM.

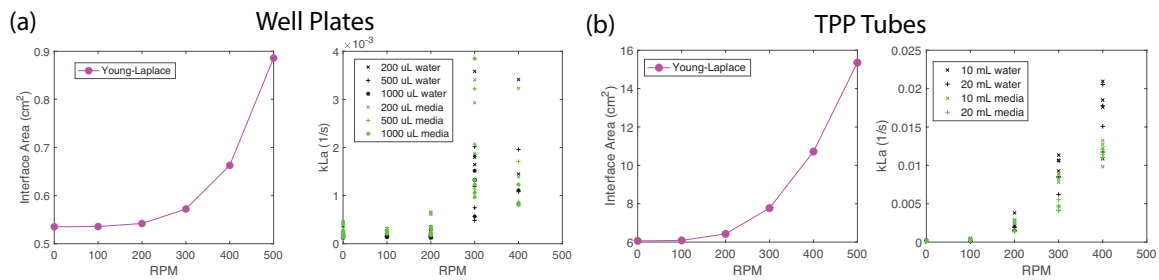


**Figure 3.6: TPP tube predictions. (a) Comparison of rise height  $H_L$  between experiments and models for the TPP tube case. The inset shows a comparison between an experimental image and the predicted interface (Young-Laplace) at 200 RPM. (b) Predictions of interface shape from the three models for 300 RPM. (c) Interfacial area prediction from Young-Laplace model.**

### 3.4. Discussion

Ultimately, for the range of Merck parameters studied herein, we have shown that the Young-Laplace model is suitable for predicting the fluid response to agitation in both the well plate and TPP tube geometries. The simpler quasi-static model is appropriate for the larger scale TPP tubes where the meniscus plays a less significant role in defining the overall surface shape. Whether such predictions are useful in practice remains to be seen, nevertheless the quasi-static assumption proposed and validated herein does allow one to readily map between different agitation radii and frequencies through comparison of the single parameter  $F$ .

These reduced order models are able to make quantitative predictions for the interfacial area, however do not attempt to model  $k_L$  and thus cannot independently predict  $k_L a$ . However, by comparing the predicted interfacial area from the Young-Laplace model and experimental measurements of  $k_L a$  in



**Figure 3.7: Comparison of predicted interfacial area from Young-Laplace model shown with corresponding  $k_L a$  measurements from experiment for (a) well plates and (b) TPP tubes. Increases in the predicted surface area show good correlation to the observed increases in measured  $k_L a$ .**

Figure 3.7, we see there is a notable correlation between predicted increases in area and measured increases in  $k_L a$ . For instance, significant increases above the baseline 0 RPM value for both interfacial area and  $k_L a$  are only first observed at 300 RPM for the well plates, and at 200 RPM for the TPP tubes. It is plausible that the overall interface deformation (related to  $A$ ) is intrinsically coupled to the vigor of bulk fluid motion (related to  $k_L$ ), and thus  $k_L$  and  $a$  are in fact intimately correlated at such small scales. Thus while the present models do not directly predict  $k_L a$ , it does appear they can be used to faithfully compare agitation conditions and fill levels in a relative manner, without the need for challenging experiments or expensive numerical simulation.

Future work might consider analyzing the fluid velocity fields and concomitant oxygen transport predicted via full numerical simulations to guide development of validated empirical correlations relating the forcing conditions, geometry, and fluid parameters to  $k_L$  in small-scale bioreactors.

## 4. Basilisk Modelling

### 4.1. Overview

A computational component has been developed as part of Phase 1b in order to generate new capabilities in both measurement and quantification of oxygen transport in the target geometries and flow regimes. Accurate numerical treatment would allow the detailed study of flow features outside the reach or range of validity of analytical modelling tools, while still in need of validation and at a higher anticipated computational cost. With appropriate data management, such a tool is also envisioned to provide access to flow quantities of interest at any point in space and time, thus strongly augmenting flow monitoring capabilities with virtual sensors that are not affected by some of the real-life challenges encountered in experimental contexts. The direct numerical simulation structure constructed herein uses the open-source code <http://basilisk.fr/> as a starting point. Boasting second-order accuracy in both space and time, adaptive mesh refinement and parallelisation options, it is an excellent foundation for our complex three-dimensional interfacial flow study, and has been a pillar in the computational fluid dynamics community for over 20 years [18,19,20]. Grounded in the interface-capturing volume-of-fluid (VoF) method [14] (elaborated on in subsection 4.2.1) and making use of very recent functionality in terms of advection-diffusion dynamics [11,12] (expanded on in subsection 4.2.3), the dedicated Basilisk code constructed for Phase 1b is intended to bridge our understanding and insight into the flow behavior in the target geometries and regimes.

This Section of the report is structured as follows: following on from this introduction, the numerical methodology employed is described in Section 4.2, including both hydrodynamic and transport aspects. Results are then summarised in Section 4.3, followed by conclusions in Section 4.4. Section 4.5 is provided to highlight the code and data provision plan. External hyperlinks are provided to relevant addition sources.

### 4.2. Methodology

Direct numerical simulation techniques are motivated by the need to accurately simulate the nonlinear conservation of momentum and mass equations that govern fluid motion, the starting point of most fluid dynamical problems in the continuum regime.

The Navier-Stokes (NS) equations are given in expression 4.1, where  $D_{ij} \equiv (\partial_i u_j + \partial_j u_i)/2$  is the deformation stress tensor,  $\rho, \mu$  and  $\sigma$  the density, viscosity and surface tension respectively,  $\kappa$  and  $\mathbf{n}$  the curvature and normal vector of the interface respectively,  $\delta_s$  the Dirac delta function that takes a value of 1 in interfacial cells and 0 elsewhere such that the surface tension term only applies at the interface, and  $\mathbf{F}$  is any other body force such as gravity:

$$\rho(\partial_t \mathbf{u} + \mathbf{u} \cdot \nabla \mathbf{u}) = -\nabla p + \nabla \cdot (2\mu \mathbf{D}) + \sigma \kappa \delta_s \mathbf{n} + \mathbf{F} \quad (4.1)$$

$$\nabla \cdot \mathbf{u} = 0$$

For multiphase flow problems, on top of the standard fluid dynamics variables (such as pressure or velocity for example) required to solve these governing equations, an additional variable is required to distinguish between the fluid phases. For a two-phase case this can be a single scalar variable which takes a value of 1 in one of the phases and 0 in the other and a value between the two in interfacial regions [22,23]. This extra variable (known as a volume of fluid or VoF field) then allows other properties (such as density or viscosity) to be expressed in terms of the VoF. For example, if we denote the VoF variable via color function  $f$ , and the values of a variable (such as density or viscosity)  $X_1$  and  $X_2$  for phases 1 and 2 respectively, then we can express the variable as  $X = fX_1 + (1 - f)X_2$ . This allows us to formulate the momentum equation in the NS equations as one single equation for both phases when expressing the fluid properties in terms of this VoF variable. We then require an additional equation governing this VoF variable given by equations 4.2, which is simply a conservation equation for the VoF field, which is a requirement that in addition to conserving the overall mass the mass of each phase must be conserved:

$$\partial_t f + \nabla \cdot (\mathbf{u}f) = 0 \quad (4.2)$$

The question then arises of how to track the interface between the two phases. A commonly used technique is the level set method, first introduced by Osher and Sethian [17] in 1988, whereby the interface is defined in terms of a higher dimensional function. Specifically the function finds the signed distance from each cell to the interface. This distinguishes the different phases with positive and negative values of the distance function and thus the zero value of the function corresponds to the interface position [13]. At each time step the level set function is then advected with the flow [16]. This method is advantageous as the explicit definition of the level set function allows for convenient calculation of interface curvature and normals required for implementing surface tension and topological transitions are handled naturally as they automatically evolve as the zero contour of the level set function. The disadvantage of the level set method however is that, after the advection stage, the distance function needs to be recalculated in each time step, therefore adding to its complexity as well as introducing errors in volume conservation [13,16]. To overcome some of these disadvantages, one alternative method discussed herein, and the one used by the Basilisk solver utilised in this body of work, is the VoF method. Before progressing to the detailed VoF functionality description, it is worthwhile introducing the software platform which will act as the infrastructure methodology for the respective technique used throughout this project.

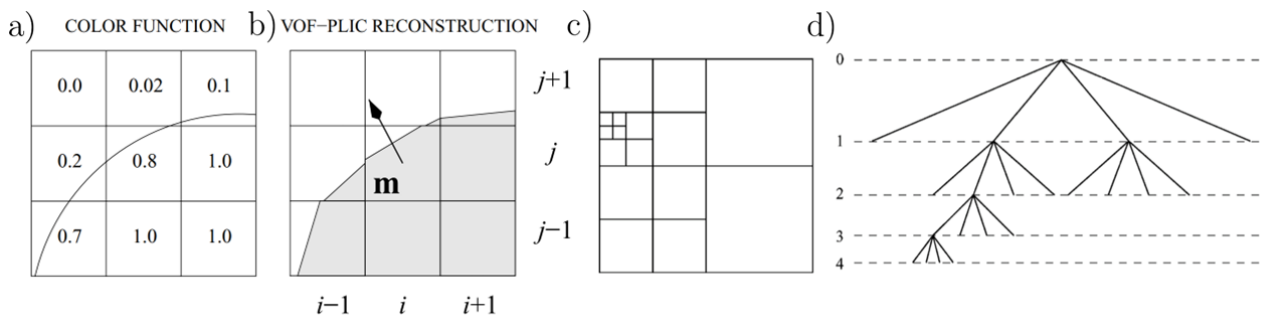
#### 4.2.1. General Computational Infrastructure

Basilisk is an open-source partial differential equation solver [21] developed as the successor to Gerris [18,19]. It is widely customisable and provides capability to handle a wide array of fluid dynamics problems, from small scale droplet impact to tsunami modelling. It has been adopted by numerous members of the fluid dynamics research community, with many examples of papers published using the framework available on the [bibliography section](#) of its website. Fundamental studies involving multi-fluid systems with interfaces have been a particular point of strength of the package, which is why the code is an ideal choice in terms of implemented methodology for interfacial flow aspects. The aforementioned VoF method is so named as it actually uses the underlying VoF field to reconstruct the



interface, and thus has the advantages of not requiring any extra fields, it naturally conserves mass due to the VoF field being governed by a conservation equation, and naturally handles topological transitions [22].

Figure 4.1 a) shows an example interface cutting through several cells as well as the values of the VoF field in each of the cells from which we reconstruct the interface.



**Figure 4.1: Demonstration of interface capturing methods for the VoF method. a) The actual interface as well as the values of the VoF field in each cell. b) Reconstruction using the piecewise linear interface construction (PLIC), where each interface section is represented by a straight line with normal direction  $\mathbf{m}$ . Example tree structure in Gerris/Basilisk showing c) the various levels of the cells, as well as d) the relationship between parent and children cells. Source: adapted from Tryggvason et al. (2011) [23] and Popinet (2003) [18].**

An accurate method of interface reconstruction makes use of the so-called piecewise linear interface construction (PLIC) [22,23] method. The interface within each grid point is still taken as a straight line segment, as shown in Fig. 4.1 b). Whilst in this case the interface is not continuous between cells, the errors are small and depend on the local curvature as well as the cell size [23]. This results in acceptable levels of accuracy [22,23], whilst still being sufficiently easy to compute. Each interfacial segment is then described by the vector equation  $\mathbf{m} \cdot \mathbf{x} = \alpha$  where  $\mathbf{m}$  is the normal to the interface,  $\mathbf{x}$  the position vector and  $\alpha$  a scalar constant to be determined. The normal vector can be found by using finite differences to find gradients in the VoF field in the neighbouring cells [23]. Once this is known the value of  $\alpha$  can be found by geometrical considerations knowing the required volume fraction in the cell [22]. After the interface is reconstructed for each interfacial cell, the VoF field is then advected in each time step by the velocity field as described in Popinet (2009) [19].

Another challenge of multiphase flows is the changing geometry of the configuration. Fluid interfaces will also be moving in time and thus one cannot know a priori where the regions of high resolution are required. The solution to this is to use adaptive mesh refinement (AMR), whereby the resolution of the grid is varied both spatially and temporally in order to focus grid points in the area of interest and thus greatly cut down on the computational cost of the simulations. Figure 4.1 c) adapted from Popinet (2003) [18] shows an example non-uniform mesh used in Basilisk. Here the mesh adopts a quadtree structure in 2D (or octree in 3D) where each square (cube in 3D) cell cell can be further split into four (eight in 3D) children cells. The entire domain is taken as resolution level zero and each splitting of the cells corresponds to an increase in the resolution level by one. Consequently, and as shown in the tree diagram in Fig. 4.1 d), the example mesh consists of one level zero cell, four level

one cells (the four quadrants), eight level two cells (the left half of the domain), four level three and four level four cells. An advantage of the tree structure utilised here is that cells which are close in the spatial domain are also stored close together within the computer memory even when the resolution changes [24]. This allows for efficient access of data between neighbouring cells required to perform calculations such as finite differences for approximating derivatives. The quad/octree structure also allows efficient access to data of all cells for given refinement levels as well as all leaf cells [18], vital when performing operations on each level sequentially such as when adapting the mesh. Further details concerning the tree structure such as the indexing method to efficiently access neighbouring cells or extension to multiple cores are readily available to the interested reader in both [tutorial](#) and publication formats [14].

---

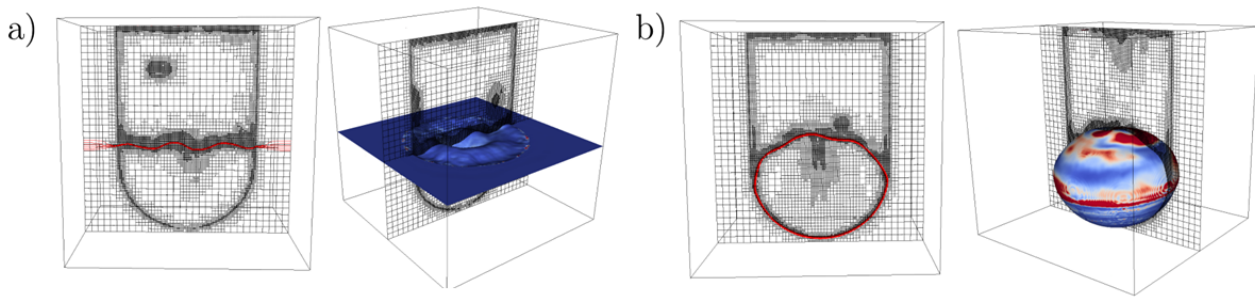
### Important

With Basilisk being an open-source software still in development stages, there is one key bottleneck affecting our target dynamics: the contact line implementation for embedded boundaries (such as the geometries given by well plates or TPP tubes) is lacking in 3D. Furthermore, compatibility issues with the other components of the package (such as transport and transfer) also need to be resolved even when this functionality becomes available. The 2D model has only been released in late 2022, while progress and testing for the 3D case is ongoing and spearheaded by groups in Paris and Sevilla, with 2024 being currently viewed as a realistic target for integration into the wider package. A robust algorithm for VoF methods and embedded boundaries in 3D is a significant research challenge in the community for a number of years and thus cannot be easily bypassed within the scope of this work package. Two compromise solutions have been identified, showcased in Figure 4.2 below:

1. **Pinning the contact line.** In this case the interface is prescribed to remain in place at the contact line, being allowed to deform away from the regions in close vicinity to the solid. While being robust, this method artificially restricts the movement of the interface, not allowing the meniscus to *climb* the geometry walls and thus being unable to achieve the oscillation-induced amplitudes observed in reality. The method imposes a 90 degree contact angle in this context.
2. **Using a superhydrophobic surface formalism.** This method effectively considers a *slippery* surface on the inside of the geometry which the interface does not touch, with the fluid instead being allowed to move freely in the volume within. Drawbacks in this case include the action of surface tension very near to regions where a triple contact line would normally exist, as well as ensuring robustness in the thin regions entrapped between the liquid and the solid.

We have opted to take the first approach in the case of the well plates given more dominant capillary forces (in view of smaller lengthscales) that would artificially curve the interface. Conversely, the more inertially-dominated TPP tube test cases are better served by the second approach, in which any local smoothing of the interface shape is comparatively negligible.

---



**Figure 4.2: Visualisation of non-uniform grid and liquid-air interfaces (slice views left, 3D views right) for a) pinned contact line and b) superhydrophobic surface specification. The interfaces are highlighted in red on the left hand side, while on the right hand side the norm of the velocity field is used to color the isosurface describing the interfaces.**

#### 4.2.2. Validation and Specifications

The combination of these above features allows for much more efficient simulations producing great improvements in the number of grid points required and thus the time to run the simulations. Fully uniform grids in 3D would be prohibitively costly, with  $\mathcal{O}(10^7)$  degrees of freedom being required at every timestep in order to ensure mesh independence in view of the target metrics. Our setup concerns two target geometries:

1. the 96-well plate geometry (an early version of which is illustrated in Fig. 4.2)
2. the TPP tube geometry (showcased for example in Fig. 4.3)

each of which is described by a reference length scale chosen to be its radius, and with a computational box size set to enable the testing of various fill levels. Through numerical experimentation it was found that at least  $2^7$  grid cells per dimension are required to ensure consistency, and  $2^8$  grid cells per dimension or more are needed for capturing finer flow features near the wall regions. This leads to simulations described by  $\mathcal{O}(10^6)$  degrees of freedom, typically executed across 16 CPUs on high performance computing clusters. Depending on the target timescale, several days of wall clock time are common for our tests. Hydrodynamic features require comparatively less time, as they are grounded in the number of periods in the orbital shaker needs to induce quasi-steady states. By contrast, oxygen transport and transfer occur over much longer timescales, and thus sufficiently many periods of oscillation need to be allowed in order to estimate  $k_L a$  values. Adjusting the timescale based on the phenomena of interest is advisable given the large disparity of resources required to study the multi-physics processes at hand.

An ideal approach beyond the scope of the present work would be a one-way coupled hybrid strategy, in which detailed flow features and quasi-periodic states are computed using the direct numerical simulation code. Should this be sufficiently well-behaved, a period could be used as repeated host flow for an actively calculated transport process, thus focusing on the longer timescales with a sufficiently

well captured background flow that does not require recomputation. The viability of this strategy depends on the target parameter and operational regimes, and would only be expected to work if the forcing induces genuinely periodic structures. Establishing whether such a flow is present can be done using comparatively quick numerical experimentation, and monitoring key norms (e.g. flow velocity component magnitudes and vorticity) alongside particle tracking features.

---

### Important

One useful flow monitoring feature is given by the use of Lagrangian particle tracking, in which we mark a specific set of starting points in the flow and monitor their evolution in time. This allows us to examine changes in locations, velocities and flow quantities of interest (such as shear stress) in an efficient manner, potentially revealing flow structures that would be difficult to detect in otherwise large datasets. To this end we use the development phase [tracer-particles.h](#) library, which has been successfully validated in a number of classical flows such as [the collision of vortex rings](#). Our aim is to use this functionality in order to reveal flow structures close to points of interest such as the bottom sensors or near side walls and/or interfacial regions.

---

### 4.2.3. Transport and Diffusion Processes

---

### Important

The standard hydrodynamic platform previously described in equations 4.1 - 4.2 requires modifications in view of the intended oxygen transfer and transport. The details below are provided in the code documentation as part of the [henry.h](#) library, which has recently been validated [11] in the context of bubble-mediated transfer in turbulent contexts, for which we refer to the [rising bubble test case](#). To our knowledge, the present project represents the first usage of this functionality outside its initial development space, thus requiring significant implementation and validation effort. Its state-of-the-art features however represented an important asset, which made it a highly informative choice in the context of a work package focused on transport/transfer processes.

---

We wish to consider the transport and diffusion of a tracer  $c$ , using different diffusion coefficients (which we henceforth denote by  $D_1$  and  $D_2$ ) and the following jump in concentration at the interface:

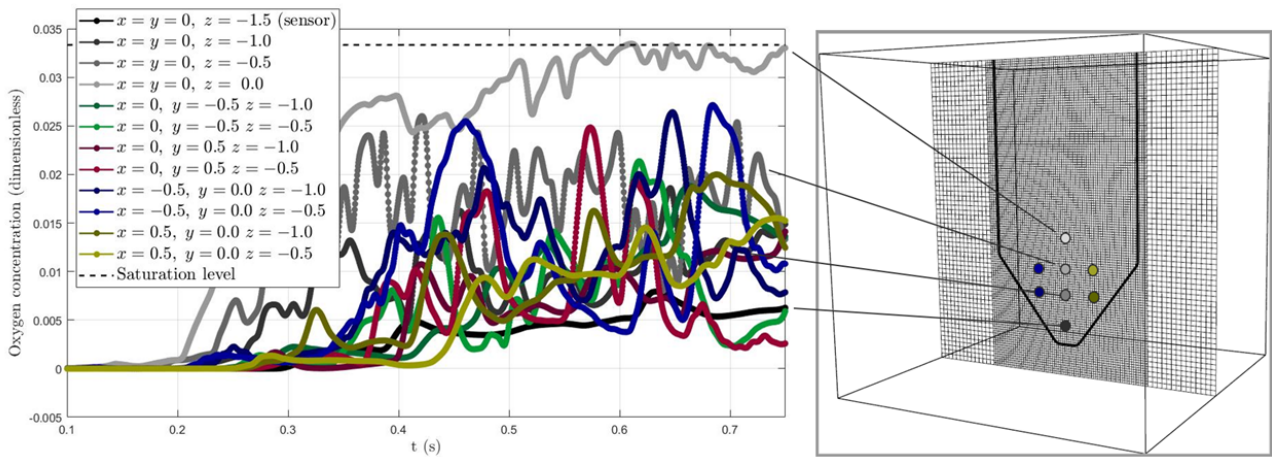
$$c_1 = \alpha c_2 \tag{4.3}$$

with  $\alpha$  denoting the proportionality constant in Henry's law, taken to be  $1/30$  in our framework. The advection-diffusion equation for  $c$  thus reads

$$\partial_t c + \nabla \cdot (\mathbf{u}c) = \nabla \cdot \left( D \nabla c - D \frac{c(\alpha - 1)}{\alpha f + (1 - f)} \nabla f \right) \quad (4.4)$$

with  $f$  as the volume fraction, and  $D = D_1 D_2 / (D_2 f + D_1 (1 - f))$  as the appropriate (harmonic) mean for the diffusion coefficients in view of stability.

The functionality above allows us to calculate (and examine) the oxygen concentration in both gas and liquid environments, keeping track of its transfer and providing measurement capabilities based on volumetric averages in order to provide a kLa value that does not require any ad-hoc expressions nor any fitting parameters. Figure 4.3 presents the raw oxygen concentration measurement at several such stations, showcasing how the upper layers are first reached by the oxygen, but with the shaking introducing complex oscillatory dynamics.



**Figure 4.3:** Example measurement output from several measurement stations inside the flow, highlighting oxygen levels at each station relative to the saturation level indicated by the dashed line. The bottom measurement station was built to replicate the position of the sensors in the experimental setup.

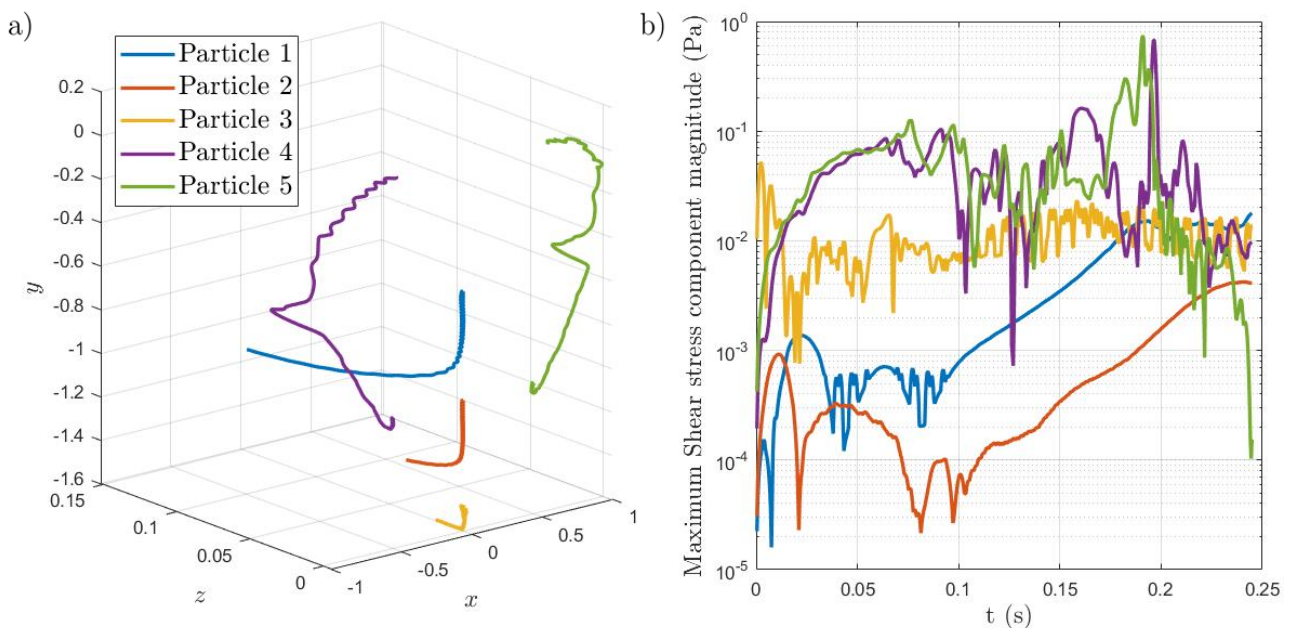
## 4.3. Results

The paragraphs below provide a comprehensive visual guide into some of the key results obtained using the previously described methodology. We first concentrate on hydrodynamic flow aspects in subsection 4.3.1 before turning our attention to the longer timescales of oxygen transport in subsection 4.3.2. Comparisons to experimental results presented earlier in this report are provided where possible.

### 4.3.1. Hydrodynamic behaviour

We begin with an inspection of the capabilities designed for measuring quantities in the flow as host background for the oxygen transport process. In Figure 4.4 we illustrate the three-dimensional trajectories of seeded Lagrangian particles inside the flow, alongside the maximum shear stress component they experience. The three particles on initialised on the central axis undergo a rotational motion to start with, followed by drifting towards one of the TPP tube walls. The asymmetrically initialised particles cross the width of the TPP tube and eventually travel towards the interface, where

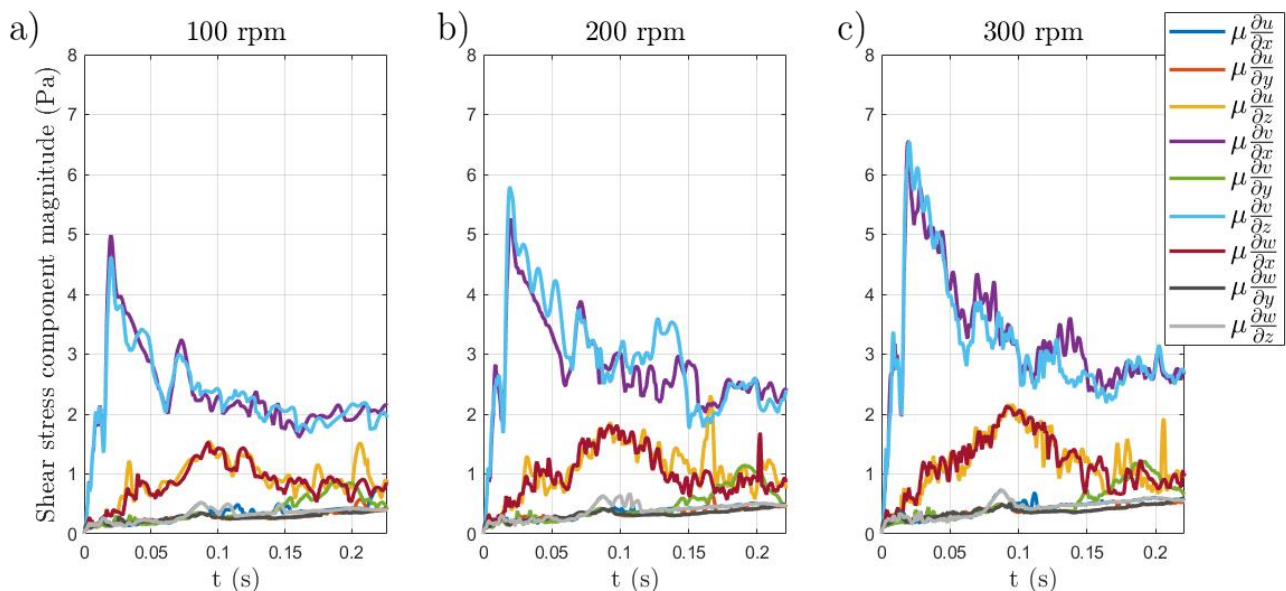
the signature of rotational motion is once again visible in their oscillatory trajectories. Due to its proximity to the wall, the bottom particle (close to the sensor location, visualised in yellow) experiences high shear stress from the onset at a level which is maintained throughout. By contrast, the other particles have periods of time during which they experience comparatively less shear stress due to their relative distance from the inner walls of the tube. Periods of shear are nevertheless experienced (see consistent increase in blue and red particle shear stresses) as more violent flow regions are traversed. All in all such a particle travel map and associated measured quantities reveal a rich flow with varied dynamics for a hypothetical cell population inside the studied geometry.



**Figure 4.4:** a) Five example particle trajectories for a TPP tube case with fill level 10 mL at 300 rpm and water as a working fluid. b) Maximum shear stress component magnitude, as encountered by each particle in its trajectory over the illustrated timescale.

A broader look at the shear stress however, as shown in Figure 4.5, allows us to inspect the behavior at the level of the entire flow field, given we have the ability to monitor components separately and capture average as well as extremal behaviors. We focus here on the TPP tube case at 10 mL fill level, and inspect three different rpm values. We concentrate on the maximum value of each stress component as a function of time experienced in the entire domain irrespective of its location. We find that certain components (e.g.  $\mu \frac{\partial v}{\partial x}$  and  $\mu \frac{\partial v}{\partial z}$ ) experience strong initial transients, followed by settling into a more stable pattern, as other components progressively converge to their equilibrium variation regions during the oscillatory motion. Ultimately the flows do settle into relatively regular motion patterns, with each increase of 100 rpm contributing to an increased of approximately 15-20% in the observed values. Comparatively lower values are observed in the well plate scenarios, with smaller typical velocities (and a smoother geometry) leading to reduced shear stress levels by up to one order of magnitude. Higher RPM values nevertheless translate to higher observed shear stress levels.

Finally, turning our attention to interfacial quantities we underline that the contact angle implementation restrictions have significant consequences over the observed variation of the interfacial height  $H_L$ . Pinned scenarios (as used in the well plate cases) have, by design, much smaller rise heights given the only variation stems from oscillatory behavior in the center of the geometry. Modelling the walls as superhydrophobic surfaces does enable some variation, as pointed out in Figure 4.6 in comparison to experimental counterparts. The typical trends revealed are an overestimation for small rpm values given capillarity active to curve the interface near wall and induce a height variation that would be augmented. This then becomes underrepresented as rpm values increase and geometry walls cannot be climbed, with comparatively weaker centrifugal forces leading to less deformation. Very similar behavior is observed for the provided media in view of the small changes in physical properties in an otherwise Newtonian fluid formulation.

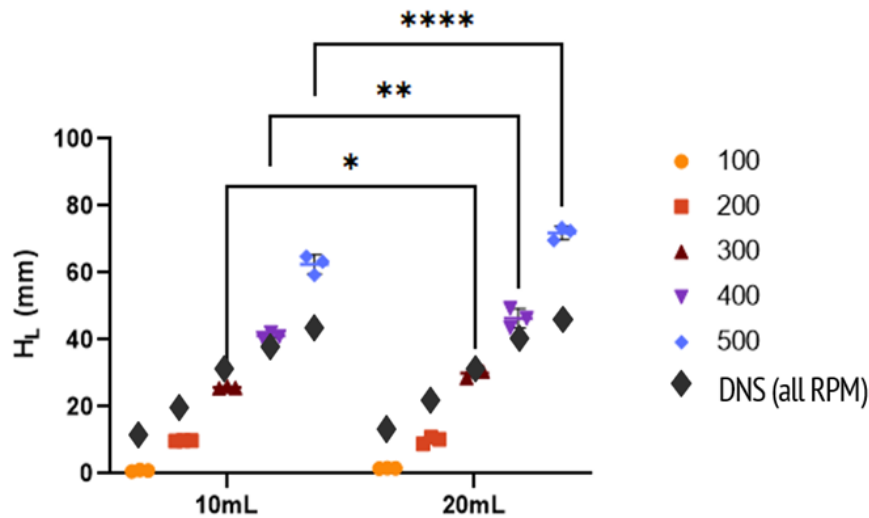


**Figure 4.5: Dimensional shear stress component value evolution at early timescales for numerical experiments performed at a) 100 rpm b) 200 rpm and c) 300 rpm for the TPP tube case at a 10 mL fill level. As anticipated, higher shear stress values are observed for higher rpm cases.**

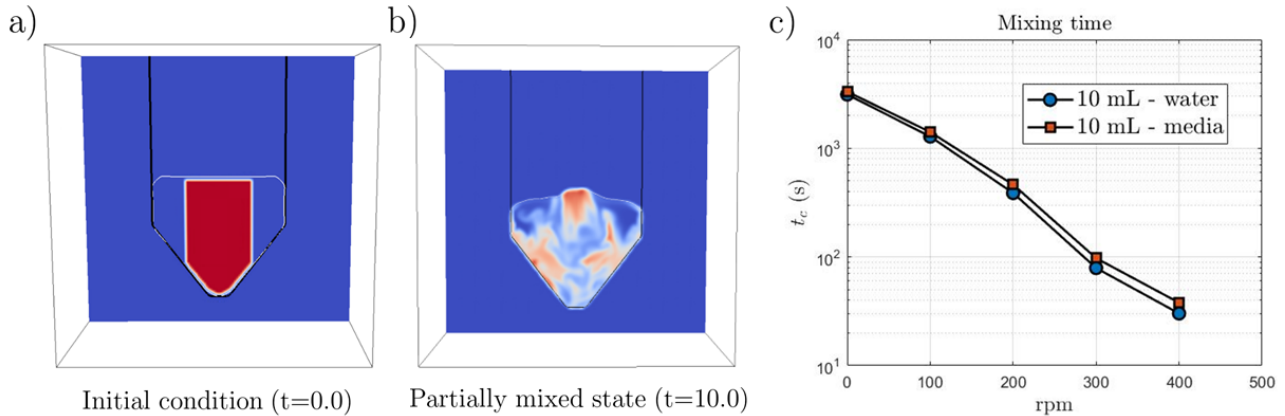
### 4.3.2. Mixing and Transport

The present subsection outlines some of the key metrics obtained from the computational platform in the context of evaluating mixing and oxygen transport. As these are processes that often occur over prohibitively large timescales - runtimes spanning more than 1 minute in real-time are extremely challenging and costly in a direct numerical simulation context - where necessary values reported herein have been constructed based on extrapolating trends observed early in the simulation cycle. A viable strategy to overcome this costly computational resource demand has been previously highlighted in the form of a one-way coupling solution using a precomputed periodic flow field and focusing on the transport process, which is one of the important recommendations in view of future research directions arising from this study.

### Conical Tube Fill Volume $H_L$ - Water



**Figure 4.6: Meniscus height measurement contrasted to the experimental study (TPP tubes, water as liquid). The black diamonds indicate direct numerical simulation results overlaid to the experimental dataset. Very similar values are obtained when changing the physical properties from water to the ones for the provided media.**



**Figure 4.7: Quantification of mixing via passive tracer placed up to half the radius of the conical tube at a) the initial time  $t=0.0$  and after b)  $t=10.0$  dimensionless time units, defined as the ratio between the radius as the reference length scale and the imposed shaking motion velocity, inside TPP tube geometries. When summarised, the full dataset reveals c) an expected trend of decreasing time required  $t$  achieve a target 95% fixedness state as the RPM values are increased**

In the context of mixing, we employ a variance-based metric in order to evaluate how mixed (or unmixed) a given state it, starting from an initial concentration field which is prescribed to occupy the column spanning up to half a radius of the target geometry (see e.g. Fig. 4.7a) for the TPP tube case). Using  $\chi(t) = 1 - \sigma^2(t)/\sigma_{\max}^2$ , with  $\sigma^2 \equiv \langle c_i^2 \rangle - \langle c_i \rangle^2$  for tracer field  $c_i$ , we note that the maximum variance  $\sigma_{\max}^2$  represents a perfectly segregated state, while  $\sigma^2 = 0$  (and consequently  $\chi = 1$ ) is indicative of a perfectly mixed state. This type of evaluation is common in the mixing literature [15], but viable alternatives do exist or can be constructed to restrict interest to a particular spatial region



for example. A mixedness level of 95% is often considered a robust target for declaring a system to be sufficiently well-mixed.

---

### Important

The time and spatial extent of the tracer placement does affect the results. For data reported in Fig. 4.7c) the half-radius width column condition at initial time  $t = 0.0$  has been used throughout, however variations (e.g. imposing a spherical passive tracer initial condition) are likely to lead to small variations in the target mixing times.

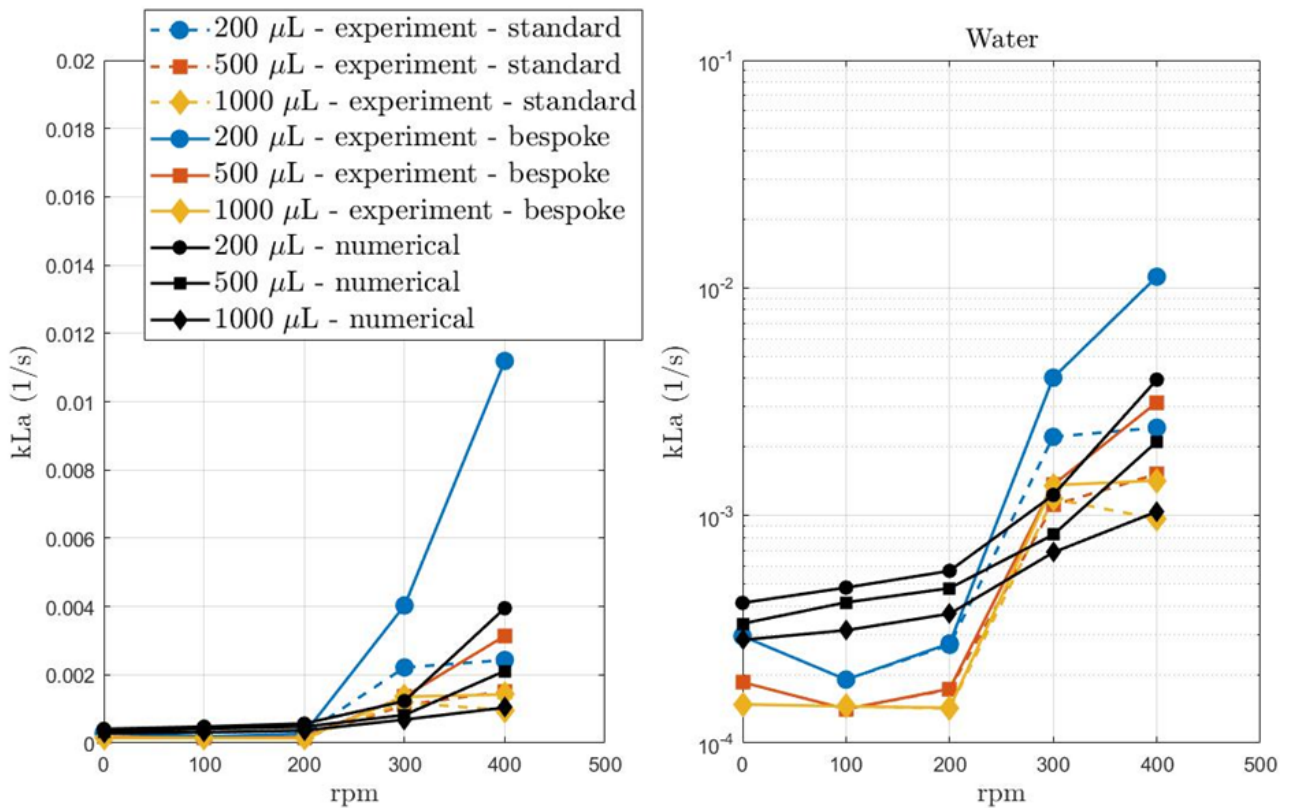
---

We find a progressively improved mixing time with RPM increase, perhaps unsurprising given the additional imposed fluid motion. Media fluid requires slightly longer timescales to mix compared to water, which we speculatively attribute to the larger viscosity slowing down the fluid motion and the stirring process. Estimated mixing times in the well plate test cases are roughly one order of magnitude higher in view of the relatively gentler motion given the smaller length scales and increased influence of viscosity in this regime. We however retain the same trend of accelerated mixing times with increasing RPM values, similar to the TPP tube case.

Figures 4.8-4.9 represent key summary figures in terms of  $k_L a$  data comparison with experimental counterparts calculated with both standard and bespoke models in the well plate case, as explained in previous subsections. The volumetric-average based construction of the  $k_L a$  from raw oxygen concentration values as they appear inside the liquid reveal in both cases consistent increasing trends as the rpm values are increased. They are best observed in a semilog plot given the large variation in values obtained spanning approximately two orders of magnitude. The agreement with the experimental dataset is good, often revealing data points between the standard and bespoke models, which can be interpreted as maximum/minimum anticipated thresholds. Nevertheless, some discrepancies are visible, particularly for low rpm values in which the interface shape is affected in the code by the contact line functionality. These systematic differences can however be explained and the arising trends provide useful diagnostic information.

Similar comprehensive comparisons have been executed for the TPP tube case, in which both water and media  $k_L a$  dataset results are summarised in Figure 4.9. Here a slight overestimation of the results is revealed, but overall the increasing trend is again robustly recovered.

Due to the computational infrastructure being built on a Newtonian fluid formulation, only differences in density, viscosity and surface tension coefficient values are considered between our two working liquids. With density and surface tension coefficient values almost unchanged, and differences in viscosity values being relatively small, it is challenging to draw any strong conclusions when trying to differentiate between the two cases given the very similar dynamics. Adding rheological features is possible in Basilisk, see e.g. [example here for Bingham fluids](#), but it represents another frontline



**Figure 4.8: Summary  $k_L a$  values obtained in the well plate case with the water as working fluids across different rpm values and fill levels, plotted in semilog form for clarity. A consistent trend of increasing  $k_L a$  for increasing rpm values is observed, alongside good agreement with experimentally measured values.**

functionality in the code currently being built by users for specific cases and yet to be fully integrated into the broader package for compatibility. These pave the way for future non-Newtonian fluid considerations, but are likely to require non-negligible efforts in view of ensuring accuracy is maintained when all new functionality is used in unison.

Additional features have also been implemented and tested in the context of gaining further insight into scenarios of interest:

- A sink term for oxygen can be imposed anywhere in the flow, representing a cell uptake rate. While highly localised uptake (e.g. at the bottom of the geometry near the sensor) can be considered, tests with a uniform uptake rate across the entire fluid volume have been performed, with an anticipated proportional decrease in  $k_L a$  values resulting from the affected transfer process.
- Near-resonance scenarios observed in experiments (e.g. TPP tube 300 rpm case) have also been tested in Basilisk. While enriched dynamics is observed, resulting in an approximate 8.7% increase in the  $k_L a$  estimate as a result of additional interfacial deformation given by the action of secondary harmonics, the contact line motion restrictions likely result in the under manifestation of such effects.

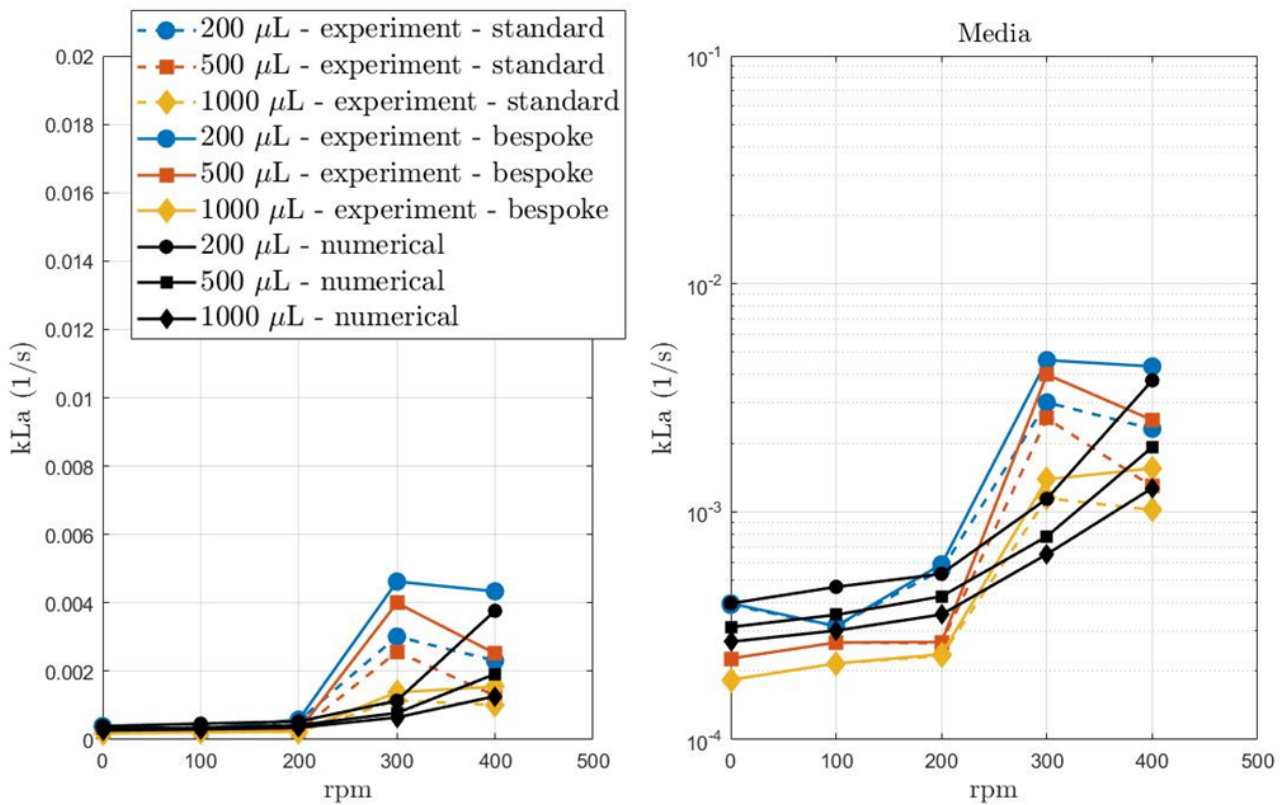


Figure 4.9: Summary  $k_L a$  values obtained in the well plate case with the provided media as working fluids across different rpm values and fill levels, plotted in semilog form for clarity. A consistent trend of increasing  $k_L a$  for increasing rpm values is observed, alongside good agreement with experimentally measured values.

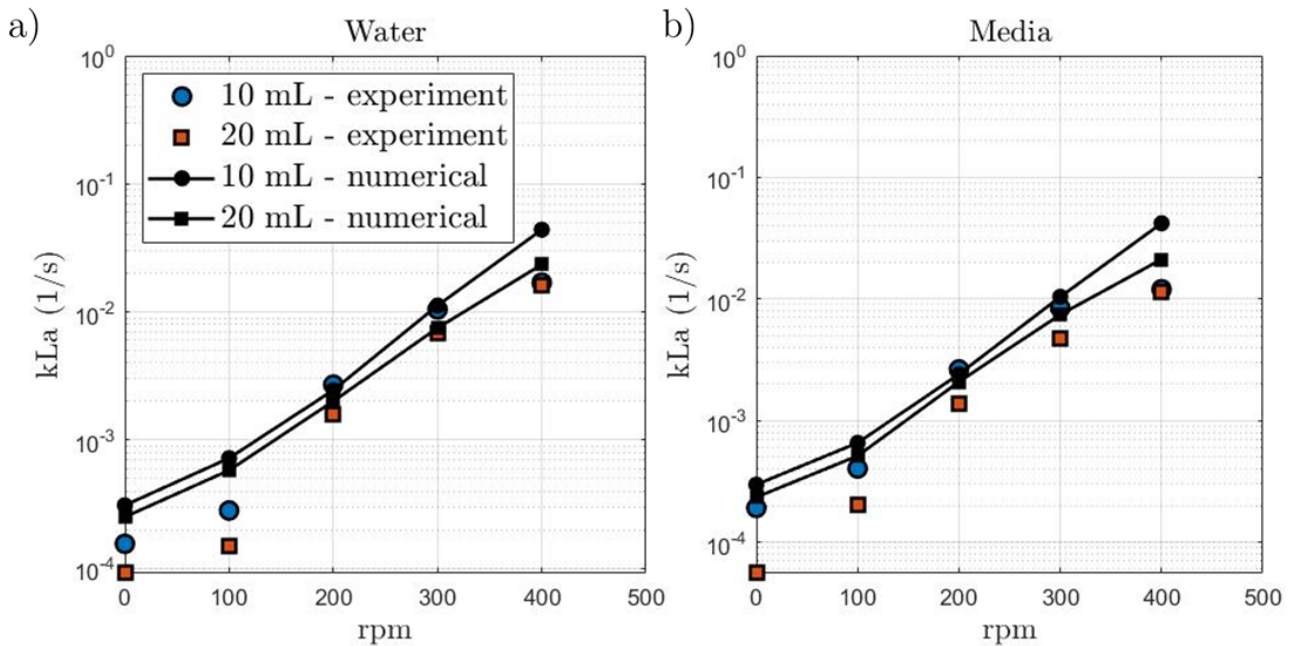


Figure 4.10: Summary  $k_L a$  values obtained in the TPP tube case with the a) water and b) the provided media as working fluids across different rpm values and fill levels, plotted in semilog form for clarity. A consistent trend of increasing  $k_L a$  for increasing rpm values is observed, alongside good agreement with experimentally measured values.

#### 4.4. Discussion

In summary, the implementation has proven to be a powerful tool capable of providing insight into some of the fundamental processes involved in oxygen transfer in the target regime. The strength of the platform lies in its fundamentals (the underlying equations being solved and the robust formulation), while losing some of its capabilities in view of specialisation towards geometries that require the imposition of 3D embedded solids. If used to target understanding and trend recovery, it can be thought of as a reliable digital counterpart to a physical system, however care must be exercised in drawing conclusions from regimes near its range of validity.

The infrastructure has the following advantages and capabilities:

- State-of-the-art advection-diffusion implementation for oxygen transfer, with stronger interfacial transfer features.
- Results follow experimental trends and allow for more targeted queries in order to identify key mechanisms and timescales, which we have taken advantage of in examining flow results.
- Access to any quantity of interest at any point in space and time, as long as we have embedded the respective quantity in the output pipeline. This proves valuable in view of sensor placement if used either as pre-experimental campaign or diagnostic tool.
- Fully open-source platform, meaning dedicated features can be added given sufficient time and effort provision. This makes adding e.g. rheological features or agent-based modelling elements on top tractable in principle.

Some of the drawbacks of the constructed framework are given by:

- Highly expensive in terms of computational runtime –  $O(1000)$  CPU hours per run (even when executed in parallel), and data-rich. A data plan is discussed as part of Section 4.5.
- Knowledge in scientific computing, HPC management and data processing required given the lack of e.g. a GUI. Minimal support outside a friendly community of benevolent users (no cost, no guaranteed support).
- Several bleeding edge features, e.g. contact line functionality in 3D, with variable and often unpredictable timescales for updates. The functionality provision is balanced by a need to maintain the package as new features are integrated and own development work needs to be made cross-compatible.

Improving features and functionality, as well as augmented versions of the code specialised to other flow regimes or rheologies, would enable further study with the same level of detail in order to inform

design pipelines. The balance between accuracy and speed, as well as generating informative datasets are non-negligible challenges that require both experience and adaptivity to the specific test cases the code is applied to. With the above in mind, the framework becomes a valuable tool that could bypass some of the traditional assumptions-limited analytical approaches and can provide substantial information in areas where experimental measurement is not possible. This platform lives best at their intersection, with modelling tools offering direction and validation data in regimes where it is valid, with experimental data providing grounding and benchmark data to build and expand from.

#### 4.5. Code and Data Transfer

The report herein is accompanied by provision of code and corresponding datasets. The key principle behind the provided implementation was to ensure enough information for a knowledgeable practitioner with high performance computing expertise to be able to take advantage of an accelerated learning curve. The source files are provided via commented source code (C language) and corresponding shell scripts required to run the direct numerical simulation either individually or as a family of tests. Brief installation instructions, a demo case with tractable runtime, and associated tutorial are provided to illustrate the execution pipeline.

For each individual simulation (approximately 50 across well plate and TPP tube parameter studies) the following datasets are made available:

- Full simulation slices ( $\times 10$ )  $\approx 1$  Gb each, accessible via dedicated visualisation tools such as bView, jView or GfsView, all of which require local installation.
- At a subset of the key measurement stations ( $\times 50$  per run and 0.01 time frequency): pressure, velocity components, oxygen concentration, passive tracer values  $\approx 10$  Mb per data file  $\times 50 \approx 500$  Mb.
- Liquid-gas interface shape files ( $x$ -,  $y$ -,  $z$ -coordinates with 0.1 time frequency)  $\approx 1$  Mb each,  $\approx 200$  Mb in total.
- 10 Lagrangian particle trajectories ( $t$ -,  $x$ -,  $y$ -,  $z$ -coordinates with 0.01 time frequency)  $\approx 20$  Mb.

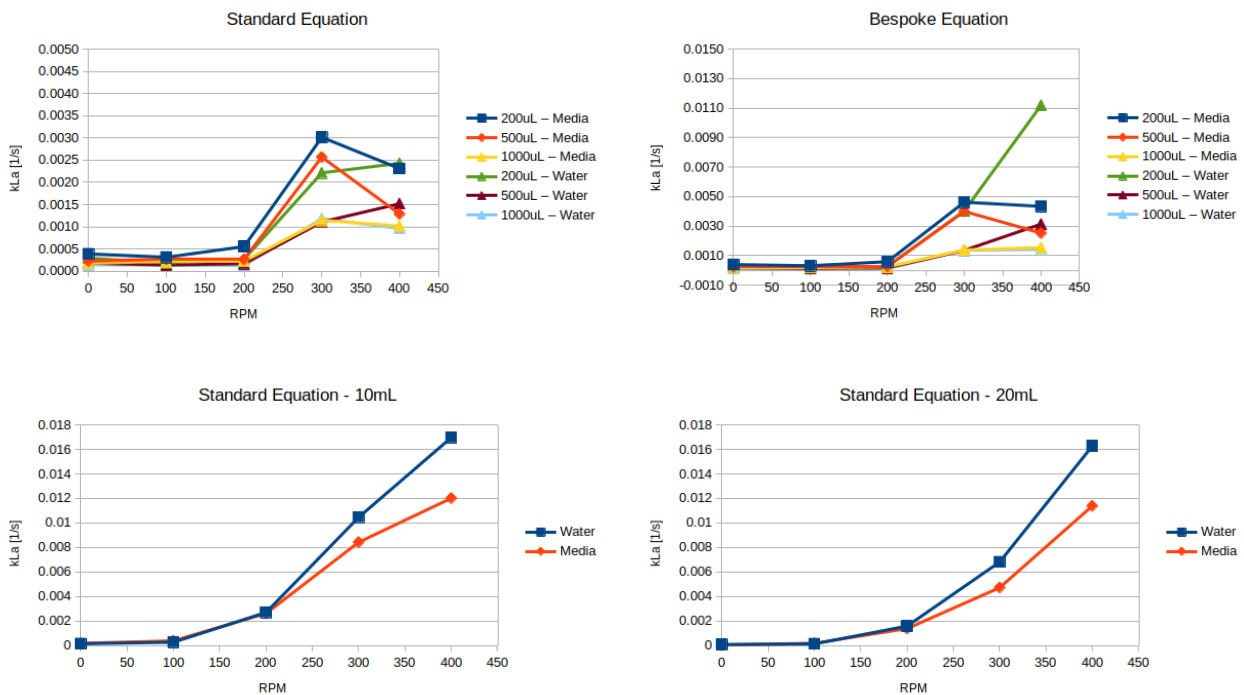
The dataset thus encompasses approximately 500 Gb in size, via Google Drive sharing like on a per case basis, in the order requested. At the level of full test suites (well plates and TPP tubes), summary information (in the form of data tables) will be provided for:

- kLa values.
- mixing times.
- maximum shear stress values.

These are intended to reflect portable and informative metrics with low data storage, leading to a total size of less than 1 Mb, thus allowing quick inspection.

## 5. Summary & Recommendations

The primary objective of this activity was to determine the different oxygen mass transfer performance of the 96 well plates and the TPP tubes in the context of being responsible for differing cell growth performance. Figure 5.1, below, replicates the mass transfer coefficient plots from Section 2. If we consider well plate operation at  $200\mu L$  fill volume and  $\geq 300$  RPM, the likely minimum value of  $k_L a$ , using the standard method, is  $0.002$  1/s. The TPP tube results indicate that at a fill level of  $20\text{mL}$  and an  $\text{RPM} \leq 200$ , the  $k_L a$  will be below  $0.002$  1/s. It is therefore plausible for oxygen mass transfer to be responsible for cell growth performance differences in the 96 well plates and TPP tubes, depending on the operational conditions applied. It would be therefore be sensible to compare  $k_L a$  values of intended operation conditions across well plate and TPP tube cell growth processes to ensure that the values are maintained when moving between scales.



**Figure 5.1: Mass transfer coefficients from 96 well plates (top row) and TPP tubes (bottom row)**

From the perspective of mixing performance, the Basilisk results suggest that the mixing time in the well plates is roughly ten times slower than in TPP tubes, due to the lower agitation at the smaller scales. The shear stress on representative non-inertial particles has also been reported, showing expected variation with RPM. Both of these metrics may provide further insight should cell growth differences be observed in cases where the  $k_L a$  values are shown to be equivalent.

The dynamic method of evaluating  $k_L a$  used here, through removal of oxygen from the liquid and using the absorption after re-introduction to fit to a solution of the equation for the time rate of change of dissolved oxygen in a well mixed case, presented specific challenges with regards shaking

stability of the table on which the wells/tubes are mounted and the chamber in which the oxygen concentration is controlled. Significant effort was required to keep additional vibration to a minimum, and to measure the frequencies of such additional vibration. A quick sensitivity test using Basilisk suggested that the primary additional vibration at 20Hz could contribute up to a 10% increase in the  $k_L a$  values. The ability to test the effects of additional agitation frequencies using computational fluid dynamics models is a valuable outcome from combining experimental and computational techniques in unison.

The variability in measured  $k_L a$  values, particularly in the 96 well plates, was also a significant challenge. A possible cause is the transport of the ambient air in the chamber and into and out of the wells when it is being re-introduced to replace the nitrogen after the purging of original air. Further considerations of the design and operation of such chambers may reveal opportunities for reducing the variability seen here.

A bespoke modeling approach has been developed, building on observed characteristics from a previously published study using 96 well plates at very similar scales to those considered here. The progressive development of this approach has generated a range of models of increasing complexity, whilst providing extremely efficient operation as a result of capturing key first principles behaviour of the dynamics of the gas-liquid interface. The most complex of the models developed, the Young-Laplace model, provides the best prediction of gas-liquid interface height in the 96 well plates, whereas a less complex model, the quasi-static model, is sufficient to provide good prediction in the case of TPP tubes. These efficient, focussed models provide a good framework to build upon further to include the ability to predict mass transfer performance, with the possibility of providing a generic small scale orbitally shaken mass transfer modeling capability.

The application of the open source computational fluid dynamics toolset Basilisk to simulating the hydrodynamics and mass transfer performance of orbitally shaken bioreactors may not have been performed elsewhere prior to this study. The ability to fully resolve the dynamics of the gas-liquid interface in terms of both motion and mass transfer is a fundamental strength of this approach. The lack of robustly tested three dimensional contact line modelling at gas-liquid-solid interfaces has been a limitation.

Overall the predictive ability of Basilisk for  $k_L a$  has been shown to be good, capturing key trends and the characteristics of operation, such as RPM, at which behaviour changes occur. The lack of three dimensional contact line modelling was shown to have a more pronounced affect on well plate predictions, as would be expected due to the greater impact of contact line forces on the dynamics at this scale. The ability to simultaneously predict mass transfer performance, mixing time and shear stress is a strength of this approach, as is the ability to consider the specific agitations conditions that may exist in practice. Subsequent work would be best placed developing a three dimensional contact line modelling capability, which could be well validated with the experimental data generated here.

## 6. References

- [1] Tschiersch H, Liebsch G, Borisjuk L, Stangelmayer A, Rolletschek H (2012) An imaging method for oxygen distribution, respiration and photosynthesis at a microscopic level of resolution. *New Phytologist*, 196(3):926–936.
- [2] Gandhi AB, Gupta PP, Joshi JB, Jayaraman VK, Kulkarni BD (2009) Development of unified correlations for volumetric mass-transfer coefficient and effective interfacial area in bubble column reactors for various gas– liquid systems using support vector regression. *Industrial & engineering chemistry research*, 48(9):4216–4236.
- [3] Maalej S, Benadda B, Otterbein M (2003) Interfacial area and volumetric mass transfer coefficient in a bubble reactor at elevated pressures. *Chemical Engineering Science*, 58(11):2365–2376.
- [4] Mohseni S, Khoshfetrat AB, Rahbarghazi R, Khodabakhshaghdam S, Kaleybar LS (2023) Influence of shear force on ex vivo expansion of hematopoietic model cells in a stirred tank bioreactor. *Journal of Biological Engineering*, 17(1):1–10.
- [5] Lee AA, Graham DA, Dela Cruz S, Ratcliffe A, Karlon WJ (2002) Fluid shear stress-induced alignment of cultured vascular smooth muscle cells. *Journal of Biomechanical Engineering*, 124(1):37–43. <https://doi.org/10.1115/1.1427697>
- [6] Fu L, Li P, Li H, Gao C, Yang Z, Zhao T, Chen W, Liao Z, Peng Y, Cao F (2021) The application of bioreactors for cartilage tissue engineering: advances, limitations, and future perspectives. *Stem Cells International*, 2021.
- [7] Alpresa, P., Sherwin, S., Weinberg, P. and van Reeuwijk, M., 2018. Orbitally shaken shallow fluid layers. I. Regime classification. *Physics of Fluids*, 30(3).
- [8] Reclari, M., 2013. Hydrodynamics of orbital shaken bioreactors (Tech. Rep.). EPFL.
- [9] Reclari, M., Dreyer, M., Tissot, S., Obreschkow, D., Wurm, F.M. and Farhat, M., 2014. Surface wave dynamics in orbital shaken cylindrical containers. *Physics of Fluids*, 26(5).
- [10] Hermann, R., Lehmann, M. and Büchs, J., 2003. Characterization of gas–liquid mass transfer phenomena in microtiter plates. *Biotechnology and bioengineering*, 81(2), pp.178-186.
- [11] Farsoiya, P.K., Magdelaine, Q., Antkowiak, A., Popinet, S. and Deike, L., 2023. Direct numerical simulations of bubble-mediated gas transfer and dissolution in quiescent and turbulent flows. *Journal of Fluid Mechanics*, 954, p.A29.



- [12] Farsoiyya, P.K., Popinet, S. and Deike, L., 2021. Bubble-mediated transfer of dilute gas in turbulence. *Journal of Fluid Mechanics*, 920, p.A34.
- [13] Gibou, F., Fedkiw, R. and Osher, S., 2018. A review of level-set methods and some recent applications. *Journal of Computational Physics*, 353, pp.82-109.
- [14] Hirt, C.W. and Nichols, B.D., 1981. Volume of fluid (VOF) method for the dynamics of free boundaries. *Journal of computational physics*, 39(1), pp.201-225.
- [15] Jha, B., Cueto-Felgueroso, L. and Juanes, R., 2011. Fluid mixing from viscous fingering. *Physical review letters*, 106(19), p.194502.
- [16] Mirjalili, S., Jain, S.S. and Dodd, M., 2017. Interface-capturing methods for two-phase flows: An overview and recent developments. *Center for Turbulence Research Annual Research Briefs*, 2017(117-135), p.13.
- [17] Osher, S. and Sethian, J.A., 1988. Fronts propagating with curvature-dependent speed: Algorithms based on Hamilton-Jacobi formulations. *Journal of computational physics*, 79(1), pp.12-49.
- [18] Popinet, S., 2003. Gerris: a tree-based adaptive solver for the incompressible Euler equations in complex geometries. *Journal of computational physics*, 190(2), pp.572-600.
- [19] Popinet, S., 2009. An accurate adaptive solver for surface-tension-driven interfacial flows. *Journal of Computational Physics*, 228(16), pp.5838-5866.
- [20] Popinet, S., 2015. A quadtree-adaptive multigrid solver for the Serre–Green–Naghdi equations. *Journal of Computational Physics*, 302, pp.336-358.
- [21] Popinet, S., 2019. Basilisk. <http://basilisk.fr>, Accessed: 2021-03-12
- [22] Scardovelli, R. and Zaleski, S., 1999. Direct numerical simulation of free-surface and interfacial flow. *Annual review of fluid mechanics*, 31(1), pp.567-603.
- [23] Tryggvason, G., Scardovelli, R. and Zaleski, S., 2011. Direct numerical simulations of gas–liquid multiphase flows. Cambridge university press.
- [24] Van Hooft, J.A., Popinet, S., Van Heerwaarden, C.C., Van der Linden, S.J., De Roode, S.R. and Van de Wiel, B.J., 2018. Towards adaptive grids for atmospheric boundary-layer simulations. *Boundary-layer meteorology*, 167, pp.421-443.
- [25] Garcia-Ochoa, F. and Gomez, E., 2009. Bioreactor scale-up and oxygen transfer rate in microbial processes: an overview. *Biotechnology advances*, 27(2), pp.153-176.